The Astrophysical Journal, 893:93 (21pp), 2020 April 20 https://doi.org/10.3847/1538-4357/ab7f2d

Localized Magnetic-field Structures and Their Boundaries in the Near-Sun Solar Wind from Parker Solar Probe Measurements

V. Krasnoselskikh[1,2], A. Larosa[1], O. Agapitov[2], T. Dudok de Wit[1], M. Moncuquet[3], F. S. Mozer[2,4], M. Stevens[5], S. D. Bale[2,4,6,7], J. Bonnell[2], C. Froment[1], K. Goetz[8], K. Goodrich[2], P. Harvey[2], J. Kasper[5,9], R. MacDowall[10], D. Malaspina[11], M. Pulupa[2], N. Raouafi[12], C. Revillet[1], M. Velli[13], and J. Wygant[8]
[1] LPC2E, CNRS and University of Orléans, 3A avenue de la Recherche Scientifique, Orléans, France; vkranos@gmail.com
[2] Space Sciences Laboratory, University of California, Berkeley, CA 94720-7450, USA
[3] LESIA, Observatoire de Paris-Meudon, Meudon, F-92195, France
[4] Physics Department, University of California, Berkeley, CA 94720-7300, USA
[5] Smithsonian Astrophysical Observatory, Cambridge, MA 02138, USA
[6] The Blackett Laboratory, Imperial College London, London, SW7 2AZ, UK
[7] School of Physics and Astronomy, Queen Mary University of London, London E1 4NS, UK
[8] School of Physics and Astronomy, University of Minnesota, Minneapolis, MN 55455, USA
[9] Climate and Space Sciences and Engineering, University of Michigan, Ann Arbor, MI 48109, USA
[10] Solar System Exploration Division, NASA/Goddard Space Flight Center, Greenbelt, MD 20771, USA
[11] Laboratory for Atmospheric and Space Physics, University of Colorado, Boulder, CO 80303, USA
[12] Johns Hopkins University, Applied Physics Laboratory, Laurel, MD, USA
[13] Institute of Geophysics & Planetary Physics, Department of Earth, Planetary & Space Sciences, University of California, Los Angeles, CA 90095-1567, USA
Received 2019 November 30; revised 2020 March 6; accepted 2020 March 10; published 2020 April 20

Abstract

One of the discoveries of the Parker Solar Probe during its first encounters with the Sun is ubiquitous presence of relatively small-scale structures standing out as sudden deflections of the magnetic field. They were named "switchbacks" since some of them show a full reversal of the radial component of the magnetic field and then return to "regular" conditions. We carried out an analysis of three typical switchback structures having different characteristics: I. Alfvénic structure, where the variations of the magnetic field components take place while conserving the magnitude of the magnetic field; II. Compressional structure, where the magnitude of the field varies together with changes of its components; and III. Structure manifesting full reversal of the magnetic field, presumably Alfvén, which is an extremal example of a switchback. We analyzed the properties of the magnetic fields of these structures and of their boundaries. Observations and analyses lead to the conclusion that they represent localized twisted magnetic tubes moving with respect to surrounding plasma. An important feature is the existence of a relatively narrow boundary layer at the surface of the tube that accommodates flowing currents. These currents are closed on the surface of the structure and typically have comparable azimuthal and tube-axis-aligned components. They are supported by the presence of an effective electric field due to strong gradients of the density and ion plasma pressure. The ion beta is typically larger inside the structure than outside. The surface of the structure may also accommodate electromagnetic waves that assist particles in carrying currents.

Unified Astronomy Thesaurus concepts: Alfven waves (23)

1. Introduction

The Parker Solar Probe (PSP) mission (Fox et al. 2015) addresses two fundamental open questions in space physics: coronal plasma heating and the acceleration of solar-wind plasmas. In both problems, wave-particle interactions involving MHD waves are known to play an important role (Coleman 1968; Belcher & Davis 1971; Heyvaerts & Priest 1983). During its first encounter with the Sun in 2018 November, PSP revealed that the nearly radial magnetic field exhibited a multitude of sudden reversals, which have been called "switchbacks" (Bale et al. 2019; Kasper et al. 2019). These structures have also been named "jets" because the (mostly radial) flow velocity is larger inside them. The typical velocity increase is of the order of the local Alfvén velocity (about 80–100 km s^{-1}).

The conditions of the solar wind during PSP's first encounter were comparable to those met by the Helios A (1974–1985) and Helios B (1976–1979) missions. PSP's closest distance to the Sun was 35.7 solar radii or 0.174 au, whereas Helios A and Helios B had perihelia of, respectively, 0.31 and 0.29 au. One of the major findings of Helios was the existence of a structured and highly intermittent solar wind alternating between fast and slow streams (Denskat et al. 1981; Marsch et al. 1981a, 1981b, 1982b; Neubauer & Barnstorf 1981). The initial studies of its magnetic field measurements focused on the presence of different types of discontinuities that were observed both in fast and slow solar winds. Neubauer & Barnstorf (1981) and Burlaga et al. (1977) classified these boundaries as tangential discontinuities (TD) when the normal component of the magnetic field is small with respect to its magnitude and as rotational discontinuities (RD) when the normal component is of the same order of magnitude as the field. An important difference between them is that boundaries of the TD type prevent mass, momentum, or energy exchange across the boundary, whereas RDs allow such exchanges. It was also noted that Alfvénic wave activity was higher in fast than in slow wind regimes (Marsch 2006). Marsch et al. (1982a) reported that at perihelion, during periods of low solar activity, the solar-wind velocity was typically 300–400 km s^{-1}, with occasional bursts up to 600 km s^{-1} that could last for a few hours. The correlation between their velocity and magnetic fluctuations, which is usually regarded as a condition for

Alfvénic-type fluctuations, was shown to be qualitatively verified for the discontinuities that were observed by Helios. According to Denskat et al. (1981), the level of Alfvén wave activity decreased with radial distance.

Interestingly, Marsch et al. (1981b) reported the existence of sudden events with "enormous deviations of the magnetic field elevation angles" of up to 45°. These were associated with deflections of the direction of the velocity vector by up to 10°. These events were arguably the earliest observations of the structures that have later been named switchbacks and have since been observed by many others (Yamauchi et al. 2004; Landi et al. 2005, 2006; Suess 2007; Gosling et al. 2009; Neugebauer 2013; Matteini et al. 2014; Borovsky 2016; Horbury et al. 2018) before PSP revealed their ubiquity in the slow solar wind. The switchbacks that have been observed by PSP during its first and third encounters are most likely the same structures as those reported by Marsch et al. (1981b) except that we can now observe them at a much earlier stage of their evolution in a near-pristine solar wind.

Another noticeable difference between Helios and PSP is the high speed of the latter, thanks to which it was almost co-rotating with the Sun during its first three encounters. Because of that, the temporal variations seen by PSP are dominated by radially moving structures and are not the spacecraft crossing spatial inhomogeneities.

During the closest approach of the first encounter, several hundred structures were observed per day, with magnetic field deviations larger than 30° and durations larger than several seconds. Surprisingly, there were very few such structures during the second encounter. Presumably, it is related to the connectivity of the satellite position during its first encounter with the equatorial coronal hole. We have analyzed in detail 20 such structures, and in the following sections, we discuss three typical structures with the aim of unravelling the properties and role of their boundaries. We intentionally selected short-duration events that last for a few minutes and avoided longer but visually more complex structures that often show the presence of substructures. Our three examples stand out by offering a sharp transition from a stationary solar wind to a regime with different properties, and then back to the initial conditions. For each of them, we pay particular attention to the characteristics of their boundaries, which are crucial for understanding mass and energy exchanges with the surrounding plasma flow.

An important question to ask of these structures' characteristics is: are they compressible or not? The first example is purely Alfvénic, with a total magnetic field that is almost constant in time. The notion of Alfvénic structure is attributed to magnetic field perturbations that satisfy two conditions. First, the variations of the magnetic field occur without the change of its magnitude, and, second, the variations of the magnetic-field vector and velocity vector happen simultaneously and satisfy the following relation:

$$\delta \boldsymbol{V} = \boldsymbol{V}_{\rm A}\frac{\delta \boldsymbol{B}}{B}\left(1 - \frac{4\pi(p_{\parallel}-p_{\perp})}{B^2}\right)^{1/2}.$$

Here, δV is the variation of the velocity vector, $V_{\rm A}$ is the Alfvén speed, B is the magnetic field, δB is the magnetic-field variation, and $p_{\parallel}$ and $p_{\perp}$ are the magnitude thermal ion pressure parallel and perpendicular, respectively, to the magnetic field.

The second structure is compressible while the third one shows a complete reversal of the magnetic field.

This article is organized as follows: after presenting the data in Section 2, we present the three examples in Sections 3.1–3.3 and subsequently discuss them in Section 4. We conclude the study in Section 5.

2. Data

In our study, we focus on in situ measurements of the magnetic field from the fluxgate Magnetometer (MAG) and the Search-Coil Magnetometer (SCM). Both are part of the FIELDS suite (Bale et al. 2016), which is devoted to the measurements of electric and magnetic fields. MAG and SCM measure three components of the magnetic field with a sampling rate of 293 samples per second. MAG, however, measures the DC field whereas the SCM only measures the AC field; the crossover between the sensitivities of the two instruments occurs between 4 and 10 Hz.

The electron density is determined from the Quasi-Thermal Noise (QTN) technique (Moncuquet et al. 2020), which uses the location of the plasma line in electric-field spectra to infer the electron density. This technique offers the advantage of providing a density estimate that is independent of calibrations and spacecraft perturbations. In the following, we average typically a few tens of spectra to reduce the noise level, so that the final time resolution of the density is 10–20 s.

The proton density and velocity are derived from moments of the proton velocity distribution as provided by the Faraday cups of the SWEAP suite (Kasper et al. 2016). A complete scan of the velocity distribution takes 0.8 s, which sets the cadence of these measurements. Their main asset with respect to the electron density is their better time resolution; therefore, we shall rely on proton data to study fast transients. Contrarily, these measurements are sensitive to the floating potential and, therefore, require inter-calibrations with other instruments. The velocity distribution also gives access to what we shall loosely call an "indication of the temperature," which is the average variance of the thermal velocity of the ions $k_{\rm B}T_i = M_i(\delta V)^2/2$; here, $k_{\rm B}$ is the Boltzmann constant.

Throughout our study, we express our data in RTN coordinates. R points from the Sun center to the spacecraft; T lies in the spacecraft plane (close to the ecliptic) and is defined as the cross product of the solar rotation axis with R, and it points in the direction of prograde rotation. N completes a right-handed system.

3. Main Properties of Switchbacks

Figure 1 illustrates the main signature of switchbacks, which is sudden deflection of the magnetic field away from the Parker spiral. During its first encounter with the Sun, PSP observed a slow but highly Alfvénic solar-wind stream for 10 consecutive days that was originating from a small equatorial coronal hole (Bale et al. 2019). The high Alfvénicity of the plasma is attested by the nearly constant total magnetic field, regardless of the variations of the individual components. The radial component of the magnetic field is, on average, negative because of the negative polarity of the field in the coronal hole. Switchbacks stand out by the rapid increase of the radial component, occasionally even leading to complete inversions of the magnetic field (Dudok de Wit et al. 2020). Their duration ranges from seconds to more than one hour.

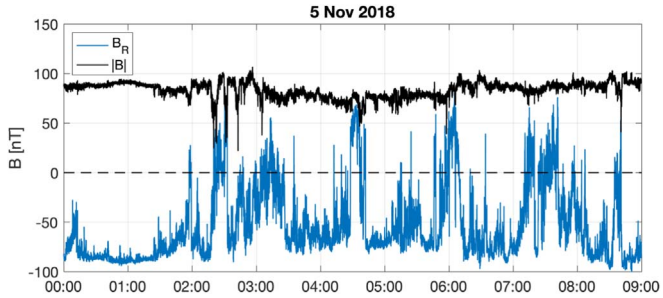

Figure 1. Magnitude (in black) and the radial component (in blue) of the magnetic field recorded on 2018 November 5 from 00:00 to 09:00 UT. Switchbacks show up as sudden increases in the radial component.

In the following subsections, we shall focus on three examples that correspond to three types of structures: first, an event that manifests pure Alfvénic properties; second, one that is compressional because the total magnetic field changes inside the structure; finally, a switchback with a full inversion of the magnetic field. Following this, we shall discuss a possible interpretation emphasizing the role of the associated currents.

3.1. Event 1—Alfvénic Structure

The first event we shall examine was observed on November 6 during the time interval from 23:32:48 to 23:39:05. The observed structure is rather typical and may be considered as representing quite a large group, if not the majority, that may be called potential magnitude Alfvénic structures. Plasma parameters for this encounter are presented in Table 1.

Figure 2 represents the data of measurements of major plasma parameters during this event. Panel (a) shows magnetic-field measurements by the MAG instrument. The data are expressed in the RTN frame (see Section 2): the subscript r stands for radial direction (blue lines), n stands for the normal one (red), and t stands for the tangential one (green). The total magnetic field is in black.

Figure 2 represents the parameters of the structure during an encounter on 2018 November 6: panel (a) shows the variations of the magnetic field in the RTN reference frame as registered by the MAG instrument. Panel (b) shows the measurements of the three components of the magnetic-field variations in the range from 5.7 to 146 Hz registered by SCM instrument. Panel (c) shows the spectra of the magnetic field obtained from SCM measurements in the same frequency range; here, the horizontal lines correspond to interferences due to the rotation of the inertial wills ensuring the pointing of the normal to the heat shield of in the direction of the Sun. Panel (d) presents an electron density as estimated from electric-field measurements using the QTN technique. Panel (e) shows three components of the proton flow velocity evaluated from SWEAP distribution function measurements. The same colors are used for velocity components as for the magnetic field: blue for radial, green for tangential, and red for normal (positive northward). Panel (f) shows proton density estimated making use of SWEAP measurements, and panel (g) shows the evaluation of the proton thermal velocity from the SWEAP instrument. In Figure 2, panel (a) shows that the encounter begins from a strong increase of the normal component of the southward-directed magnetic field. It grows from several nT to more than 50 nT, and at the same time, the magnitude of the radial component decreases from about 80 to 60 nT and then continues to decrease slowly inside the structure to about 40 nT, remaining negative for the entire time. The normal southward component of the magnetic field becomes dominant, which results in the deviation of the magnetic field to about 62° with respect to magnetic field before encounter. At the same time, the magnitude of the normal (RTN) component of the velocity shown in panel (d) of the same Figure increases from zero to about 80 km s^{-1}, and the radial component increases slightly also. The event lasts up to 23:39:04/05 when the magnetic field returns back to the value close to its initial in 5 s; the same occurs the velocity vector. It is worth noting that during all of these variations, the magnitude of the magnetic field remains almost constant, as is the case for Alfvénic structures. The second feature, with an almost synchronous variation of the velocity and the magnetic field, and with a precision of 0.3 s for particle moments evaluated from measurements by the SWEAP instrument, further validates it. Here, it is necessary to mention that an evaluation of the ion distribution function moments require 0.8 s; thus, the notion of synchronous means moments require that the two processes may be treated as such if the time shift between the FIELDS and SWEAP instruments measurements is less than 0.8 s. The two techniques used to estimate the plasma density, QTN and averaging over the ion distribution function, are complementary. QTN determines with high precision the local electron density, making use of the position of the peak in the spectra corresponding to the zero of the dielectric permittivity (Meyer-Vernet et al. 2017; Moncuquet et al. 2020). When the electron gyrofrequency is much smaller than the plasma frequency (it is our case), this peak position as a function of frequency is very close to the plasma frequency, which allows one to evaluate the plasma density with high precision. An important advantage of this technique lies in its independence of evaluation on potential of the satellite and of instrument itself. The weak point is related to the need to averaging over several tens of points in order to evaluate the position of the peak with the high precision. This leads to the smoothing of the sharp density fluctuations. The determination of the density (and other moments of the ion distribution function) making use of the Faraday cups technique (Kasper et al. 2016) is on the contrary dependent upon floating potential of the satellite and of instrument itself and also on the angular view of the instrument. From the other hand, it allows us to have more rapid measurements that are quite important in the studies of the relatively small-scale fluctuations and sharp boundaries of structures. This explains the difference of the density evaluation presented in the panels (d) and (f) of Figure 2. The thermal velocity shows up large with a sharp increase on the leading edge and a decrease on the trailing edge of the structure, and the variance inside is two times higher than that outside, which corresponds to a temperature four times higher. An estimate of the ion temperature and the plasma ion beta (using density measurements by the SWEAP instrument) shows that plasma ion beta outside the structure is about 0.36 before the encounter and about 0.6 after. The temperature inside the structure is almost four times higher; thus, the boundary according to our data represents a rather sharp transition for ion β from $\beta \simeq 0.36$ to β about 1.5. However, the total dynamic pressure remains significantly larger.

It is worth noting the presence of important perturbations of the fields, plasma density, and flow velocity in the surrounding plasma. There is rather intense wave activity just before the

Table 1
Major Plasma Parameters for the Alfvénic Structure

Parameter	Before Encounter	Inside Structure	After Encounter
Magnetic-field Vector (nT)	[−75.8;−17.5;22.5]	[−46.1;27.5;−63.6]	[−74.4;18.8;23.0]
Magnetic-field Magnitude (nT)	81.0	83	80
Velocity Vector (km s^{-1})	[323.4;26.7;31.4]	[360.3;49.6;−74.6]	[330.6;56.3;33.9]
Velocity Magnitude (km s^{-1})	326	371	337
Ion Plasma Density (cm^{-3})	324	412	361
Ion Temperature (eV)	18	57.2	28.4
Ion Beta	0.36	1.47	0.6
Ion Inertial Length c/ω_{pi} km	12.6	11.2	12.0
Ion Larmor Radius V_{Ti}/Ω_i km	5.2	9.5	6.4

leading edge of the structure, characterized by an important increase of the normal component of the magnetic field from the almost negligible value to almost 90 nT accompanied by an increase in the density, velocity, and ion temperature with a rather rapid pre-return and then slower return to previous values, where the magnetic-field magnitude is also slightly perturbed.

Now, we shall examine in more detail the boundaries of the structure. In order to do so, we use a technique called Minimum Variance Analysis (MVA). The MVA technique for the current sheets described in detail in (Sonnerup & Scheible 1998), determines three eigenvalues and corresponding eigenvectors. The largest eigenvalue shows the direction of the largest change of the magnetic field, and transformation of the field onto corresponding reference frame provides the magnitude of total magnetic-field change in the corresponding direction. The minimum variance vector determines the direction of spatial variation of the field. Since the Amper's law states that the current flows to the direction perpendicular to both the maximum jump of the field and the direction of its variation, the eigenvector corresponding to intermediate eigenvalue determines the direction of the current flow. Since the SWEAP measurements provide the flow velocity vector, its projection to the direction of the normal to the current sheet and time of the boundary crossing allow one to evaluate the characteristic spatial scale of the current sheet. Figure 3 shows the boundary transition at the leading edge of the structure and the results of the MVA of the MAG and SWEAP data. It shows the variations in the RTN frame and in the reference frame defined by MVA for the magnetic field and velocity.

The upper panel (a) of the Figure shows the variation of the magnetic field in the RTN frame as a zoom in of Figure 2 on the leading edge of the structure. The transition occurs at approximately 23:32:47/48 and in about a second, the magnitude of the normal component of the magnetic field decreases from a small positive value of about 10 nT up to −50 nT while the magnitude of the radial component at the same time decreases from about 80 nT to about 60 nT. Two components become comparable and during further slow evolution, the normal component continues to increase, the magnitude of the radial one is decreasing, and the normal component becomes dominant with a field magnitude of about 70 nT. The magnitude of the magnetic field slightly increases also from 81 nT outside to 84 nT inside the structure. Panel (b) shows variations of the magnetic-field vectors corresponding to three eigenvalues found by means of the MVA analysis. Here, the colors are used differently than in the other Figures: blue marks the component corresponding to the largest eigenvalue, i.e., corresponding to the largest variation of the field, green represents the component corresponding to an intermediate value, and red signifies the one related to the smallest eigenvalue. This last also determines the direction of the normal to the transition considered a discontinuity. Panel (c) shows the synchronously occurring evolution of the velocity vectors. Here, the radial velocity is shifted down to 300 km s^{-1}, to show the variations having comparable magnitudes. The radial velocity changes from 323 km s^{-1} outside to 360 km s^{-1} inside. The normal component of the velocity drastically changes from 22 km s^{-1} in the south–north direction to 75 km s^{-1} in the opposite north–south. The total velocity increases, and the difference corresponds approximately to Alfvén velocity. Taking into account that the magnetic field magnitude is about 81–83 nT, and the plasma density about 400 cm^{-3}, one can find that the Alfvén velocity is about 100 km s^{-1}. The SWEAP instrument data here as mentioned before is shifted to 0.3 s. For this event, we have evaluated the direction of the normal to the boundary for the velocity vector also, and it is very close to the one found for the magnetic field (within 9° of difference). Since the transition for the velocity vectors coincides with the transition for the magnetic field, MVA analysis for them is very similar to that of for magnetic field. Panel (d) shows the variation of the normal to the boundary component of the velocity that varies from about 40 km s^{-1} outside the structure to approximately 10 km s^{-1} inside but then grows to larger values. The normal vector to the structure at the leading edge is close to tangential axes with the small component along vertical, while the radial component is negligible. The normal component of the magnetic field to this boundary (panel (b) in Figure 3) is equal to $B_n = -2.5 \pm 3.2$ nT, i.e., it is practically negligible.

Figure 4 shows variations of the fields and velocities across the trailing-edge boundary. The crossing of the trailing edge takes about 2 s, a little longer than that of the leading edge, and the normal velocity is much larger than that of the leading edge; thus, the thickness of the boundary is also significantly larger. Panel (a) presents variations of the components of the magnetic field in the RTN frame. The radial component decreases from the value of about −25 to −74 nT; at the same time, the normal component returns from the large negative value of about −75 nT to a positive value of about 50 nT. The total magnetic field slightly slowly decreases also. The variations of the magnetic field in the MVA frame are presented in panel (b). The evolution of two major components of eigenvectors consists in slow rotation of the vector in clockwise direction with some wave activity around departure and arrival points. Panel (c) shows variations of the velocity vector, the radial component is downshifted to 300 km s^{-1}, the tangential component remains almost unchanged, and the radial

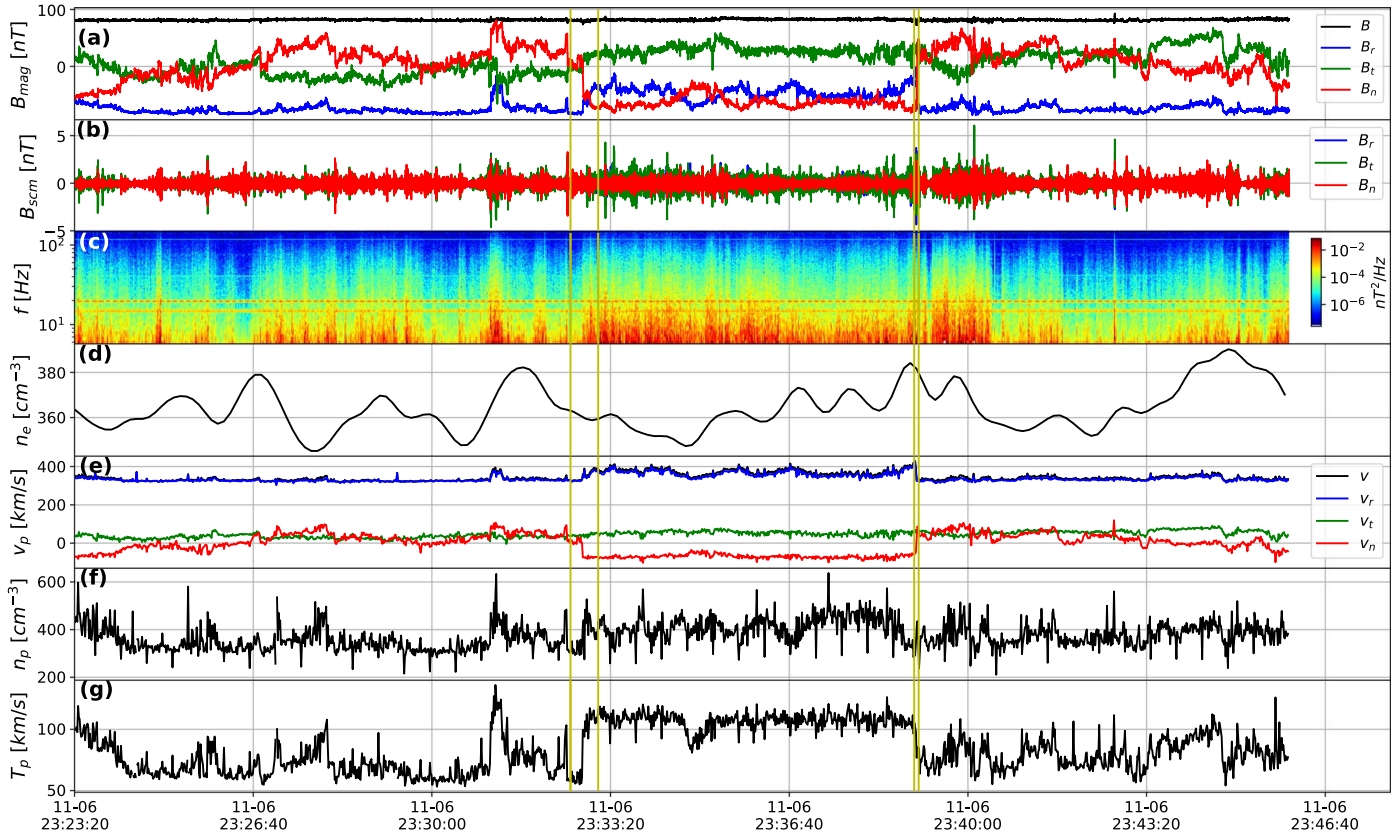

Figure 2. Alfvénic-type magnetic structure detected on 2018 November 6: Panel (a): the magnetic-field components in the RTN reference frame (the radial component is in blue, the tangential one in green, and the normal one in red). The magnetic-field magnitude is shown by the black curve. Panel (b): magnetic field fluctuations from the SCM instrument (the colors are the same as in panel (a). Panel (c): the magnetic-field fluctuations dynamics spectrum. Panel (d): the averaged electron plasma density from the QTN technique. Panel (e): the plasma flow velocity from the SWEAP instrument measurements (the components colors are the same as in panel (a). Panel (f): the ion (proton) density from the SWEAP instrument measurements. Panel (g): the ion (proton) thermal velocity from the SWEAP instrument measurements.

velocity decreases from 420 to 323 km s^{-1}. The normal component of the velocity changes from 60 km s^{-1} toward south to 80 km s^{-1} toward the north. The total velocity decreases also from 428 to 328 km s^{-1}. The normal vector to the boundary is found to be $\boldsymbol{N} = [0.48; 0.8; 0.35]$, the largest component is along the tangential axes, but the radial and normal components are also quite significant. The normal component of the magnetic field is $B_n = -13.3 \pm 5.8$ nT, still significantly smaller than the magnetic field magnitude. The variations of the magnetic field and velocity occur synchronously within the precision corresponding to a characteristic sampling rate of particle measurements. Panel (d) shows the variations of the normal velocity across the boundary. It varies in the range 200–235 km s^{-1}.

An important characteristic of the Alfvénic fluctuations consists in the linear relation between the perturbations of the velocity and the magnetic field. As it was already noted by Kasper et al. (2019), in majority of cases, they vary simultaneously, which validates the hypothesis that the fluctuations are Alfvénic. In the MHD approximation, the relation written above implies

$$\delta V = c \boldsymbol{V}_{\rm A} \frac{\delta \boldsymbol{B}}{B};$$

here, c is a constant.

In Figure 5, we present the variations of the normal components of the magnetic field and velocity that undergo the largest variations. The vertical lines show the areas of the major transition for the leading and trailing edges. The jump of the velocity on the leading-edge boundary is about $\delta \boldsymbol{V} = 100$ km s^{-1}, and the corresponding jump of the magnetic field is $\frac{\delta \boldsymbol{B}}{\boldsymbol{B}}|\boldsymbol{V}_{\rm A}| = 93$ nT; thus, the coefficient c is about 1.08, and similar values for the trailing edge $\delta \boldsymbol{V} = 141$ km s^{-1}, $\frac{\delta \boldsymbol{B}}{\boldsymbol{B}}|\boldsymbol{V}_{\rm A}| = 125$ nT, give the value 1.12. These numbers are in the range of the error bars on the actual level of instruments calibrations; thus, the coefficient is about 1.

The wave activity around the leading-edge boundary is relatively weak, but it is quite intense around the trailing edge. Figure 6 shows its manifestations around it. In the left of panel (a), the three components of magnetic field variations registered by the MAG instrument in the frequency range 1–4 Hz are presented for a short time interval around the boundary from 23:39:02 to 23:39:05; the colors are similar to those of the other Figures. The amplitudes of oscillations may become as large as 10 nT. The wave magnetic field rotates as shown on panel (b) where the hodograph of vectors corresponding to two largest eigenvalues is shown. We determine the k-vector of the wave and find that it makes an angle of 60.°5 with the boundary normal. This provides a strong indication that the wave mode corresponds to a surface wave (Hollweg 1982). This wave activity is manifested in a strong increase of the local wave energy flux.

Figure 7 represents an evaluation of the Poynting flux estimated for the time interval covering crossing of the structure. In panel (a), the magnetic field variations are shown to determine the timing and positioning of fields and the

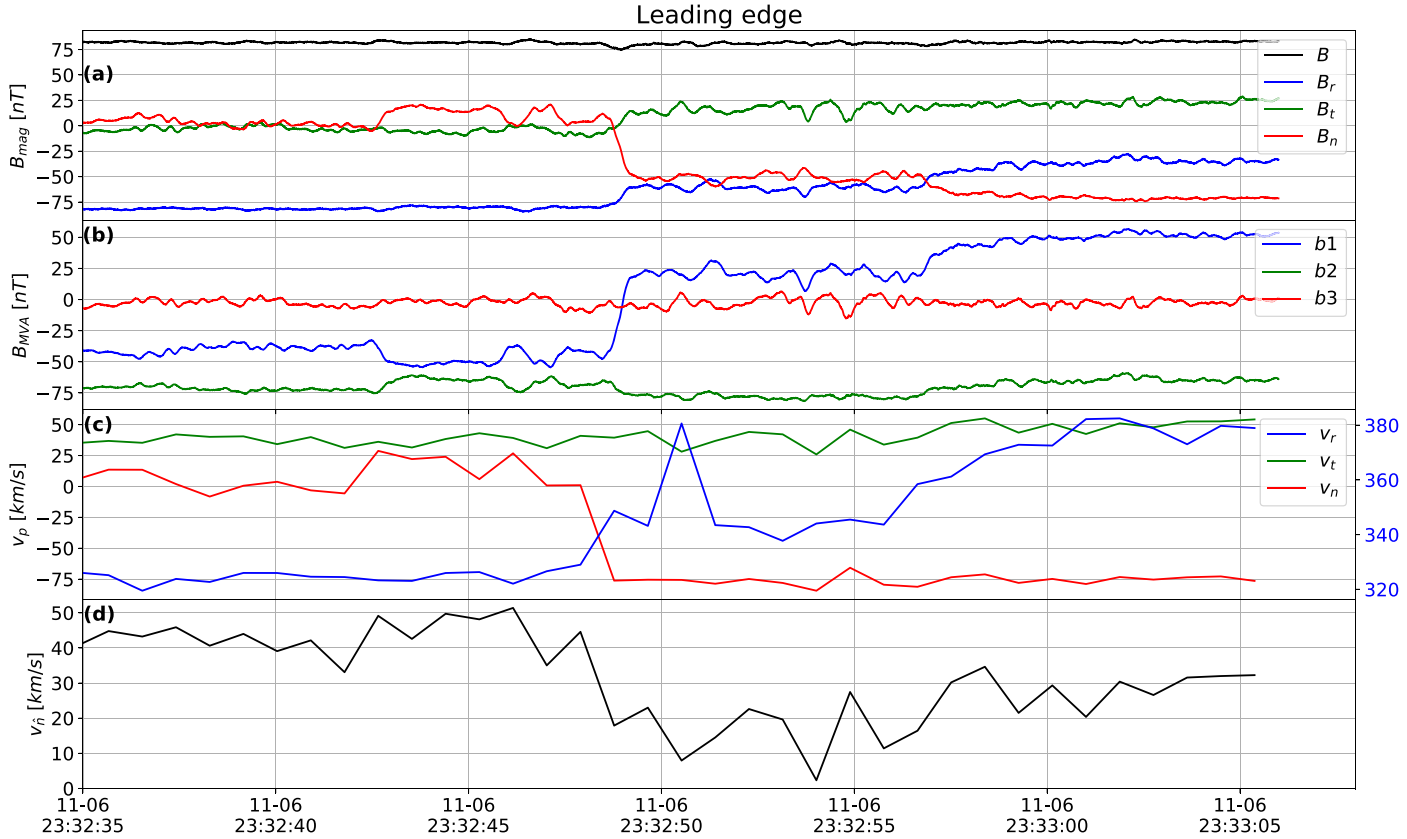

Figure 3. Magnetic field. Panel (a): in the RTN frame; panel (b): in the MVA frame) and plasma bulk velocity; panel (c): in the RTN frame and panel; panel (d): the normal to the boundary component, on the leading edge the structure shown in Figure 2. The components colors in the RTN frame are similar to the ones in Figure 2. In the MVA frame, the colors are used differently than on other Figures: blue marks the component corresponding to the largest eigenvalue, i.e., corresponding to largest variation of the field, green marks the component corresponding to intermediate value, and red signifies the one related to the smallest eigenvalue. In panel (c), the largest velocity, being strongly different from the others, is scaled on the right vertical line.

Poynting flux with respect to boundaries. The magnetic field fluctuations registered by SCM instrument are shown with the spiky bursts of large-amplitude waves in the range of several Hz on the trailing-edge boundary of the structure as well as inside it. It is worth reminding the reader that the wave activity around leading-edge boundary is significantly weaker, and the Poynting flux is also much smaller. Panel (c) represents an evaluation of the z-component of the Poynting flux calculated in the plasma reference frame. The flux calculated in the satellite reference frame might contain artificial enhancements and attenuations caused by variations of plasma speed around the satellite. Velocity variations create artificial variations of the electric field due to V cross B induced electric field, which, in its turn, results in artificial variations of the Poynting flux. In the plasma reference frame, this velocity pollution effect is excluded. The measurements of two components of the electric and magnetic fields allow one to evaluate the z-component of the Poynting flux. The procedure of the calibration of the electric field making use of the magnetic-field measurements is described in detail by Mozer et al. (2020). It is worth mentioning that the z-component in the satellite reference frame is very close to the radial direction. The Poynting flux in the overwhelming majority of events where it is significant is directed toward interplanetary space. However, there exists some quite short intervals when it is directed oppositely, toward the Sun. The intervals of sharp increase of the Poynting flux coincide with the bursts of wave activity; as it is quite intense around the trailing-edge boundary, the Poynting flux strongly increases there.

The data set presented for this event admits quite a natural interpretation of the observations in terms of the crossing of the magnetic tube as presented by the sketch in Figure 8. The characteristic spatial scales of plasma for this event are the ion Larmor radius and the ion inertial length. The ion Larmor radius varies in the range 5–9.5 km, and the ion inertial length varies in the range 11–12 km (see Table 1). These characteristic scales are significantly smaller than the scales of variation of the parameters of macroscopic plasma motions in the whole region except the boundaries. This implies that the macroscopic plasma flow may be treated in terms of "frozen in motion" and in MHD approximation. It means that the plasma moves along the field lines of the magnetic field. Our data testify that the satellite traverses the region where plasma parameters and fields strongly differ from those outside the structure. In order to better understand the physical processes related to this magnetic tube, the motion of the plasma may be separated into two parts: (1) the motion of the plasma flow along the field lines inside and outside the tube, which we shall denote as $\boldsymbol{V}_{\rm par}$, and (2) the motion of the magnetic tube itself perpendicularly to its axes, denoted correspondingly as $\boldsymbol{V}_{\perp}$.

The estimates of the velocities of the plasma flow and magnetic field tubes for the structure we examine give following results. Before the encounter, the flow moves along the field lines with the velocity 2977 km s^{-1}, and magnetic field lines (tubes) have relative velocity with respect to satellite in

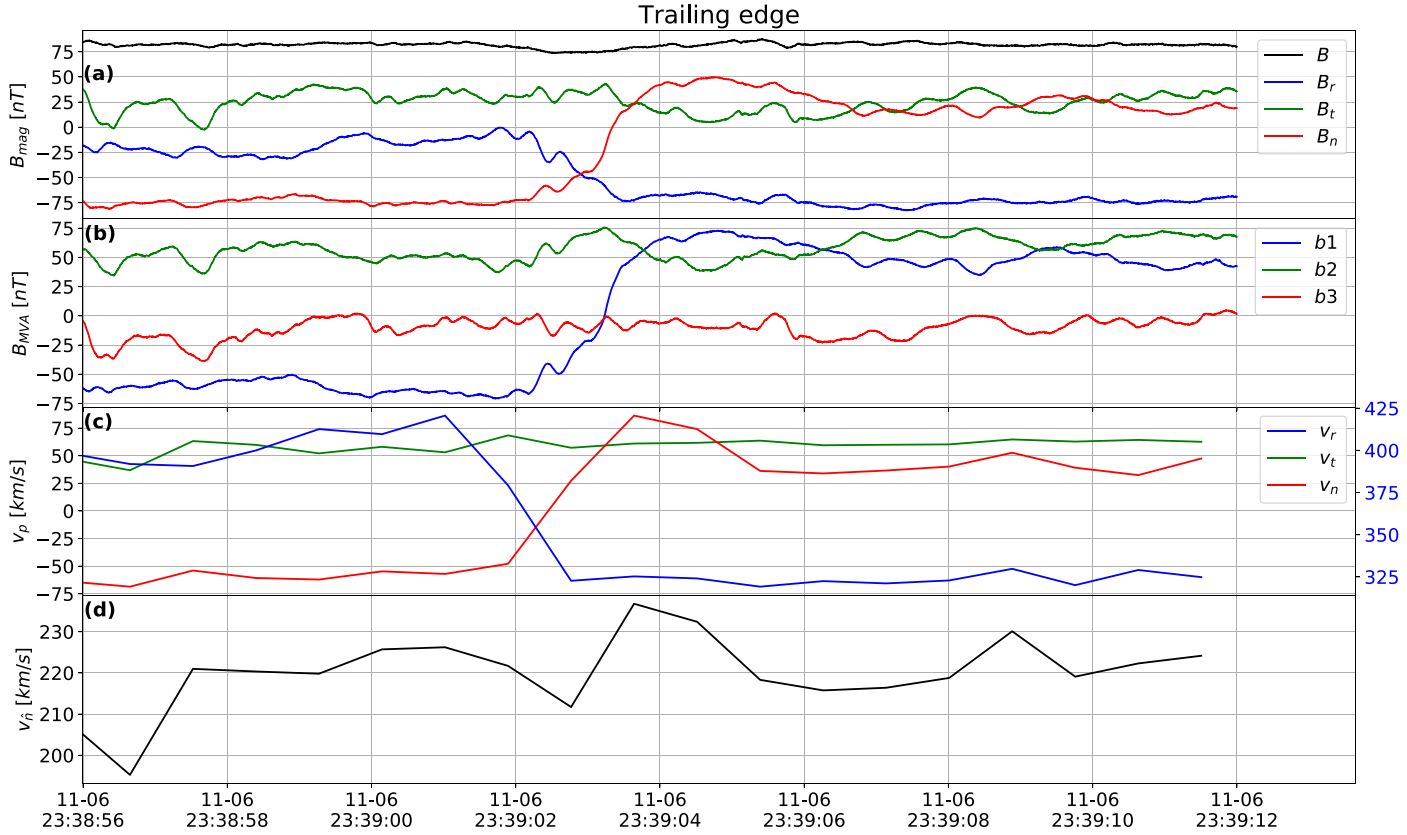

Figure 4. Magnetic field and plasma bulk velocity on the trailing edge of the structure shown in Figure 1. The format is the same as in Figure 3.

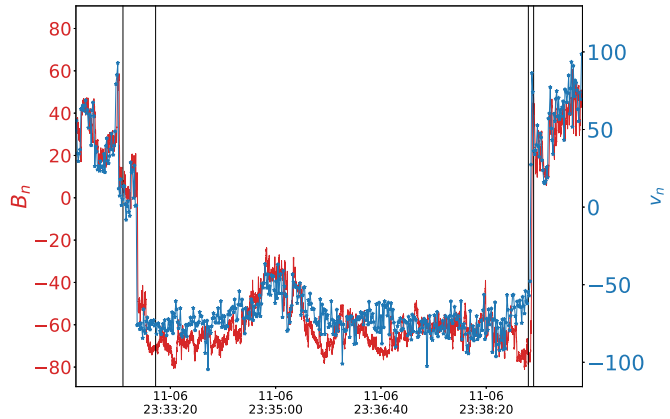

Figure 5. Normal components of the magnetic field (red) and plasma bulk velocity (blue) during crossing of the structure (Figure 2), showing linear correlation. The leading and trailing boundaries are marked by the vertical lines. The variations on the boundaries are synchronous and fit the linear relation.

the orthogonal direction equal to

$$\boldsymbol{V}_{1\perp} = [46.1;\ -35.5;\ -111.4]\ \mathrm{km\ s^{-1}}.$$

There is no way to define the tube's velocity along its axes; thus, we attribute it to the plasma flow motion. One can see that the tube lines are directed mostly radially from the Sun, and they move preferentially in the direction from north to south with some deviation toward the tangential direction. After crossing the leading edge of the structure and entering inside it, the magnetic field drastically changes its direction, and the average velocity vector also changes. Making an estimate of the velocity of the plasma flow along the field lines inside the structure, one finds it to be equal to $129.2\ \mathrm{km\ s^{-1}}$, and the velocity of the tube in the orthogonal direction is presented by the vector: $\boldsymbol{V}_{2\perp} = [287.6;\ 91.6;-172.4]$ with perpendicular velocity equal to $V_{2\perp} = 347.6\ \mathrm{km\ s^{-1}}$. Kasper et al. (2019) called such structures "jets," because the total measured velocity with respect to the external observer, in our case, the satellite, inside the structure is indeed larger than the total velocity of the flow and field lines outside the structure.

The angle between the internal and external tubes before encounter is 75°.5, and the angle with the tubes after crossing the structure is 67°.6. The magnetic field tube of the structure moves mostly in the direction of the vertical-radial plane with an angle of elevation about 51°, and its motion is mainly in the same plane in a radial direction outward and the vertical north–south direction. The relative velocity of the combined motion of the tube and plasma flow along the tube with respect to external flow before is about $113.5\ \mathrm{km\ s^{-1}}$, which is close to the local Alfvén speed.

After crossing the trailing-edge boundary, the direction of the tubes changes drastically again returning close to the initial direction. The flow velocity parallel to the local magnetic field becomes equal to $V_{\mathrm{par}} = 284\ \mathrm{km\ s^{-1}}$, and perpendicular velocity of the field lines is presented by the vector $\boldsymbol{V}_{\perp} = [209.\ 4;\ 211.5;-17.5]\ \mathrm{km\ s^{-1}}$.

Our interpretation of the structure as magnetic tube that one may imagine to be cylindrical with circular or elliptical cross section provides an idea about THE characteristic transverse scale of the structure. The normal component of the velocity along the leading edge of the structure varies from V_{lead} 10–40 $\mathrm{km\ s^{-1}}$, and during the crossing of the trailing edge, it

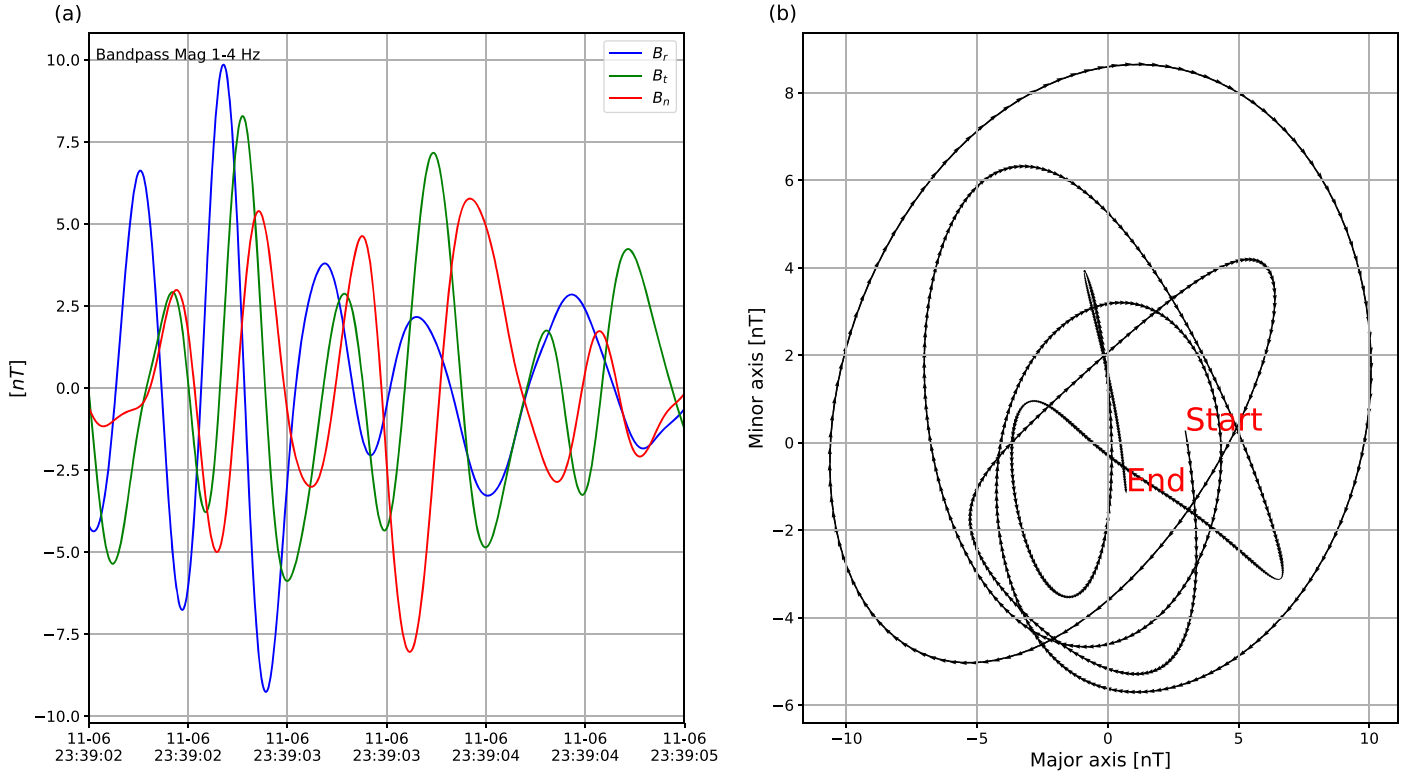

Figure 6. (a) Waveforms of the magnetic-field fluctuations in the RTN frame filtered in the 1–4 Hz frequency band and a 3 s time interval on the trailing edge of the structure are shown in Figure 2. (b) Hodograph of the magnetic field (in the plane transverse to the wave normal) showing close to the circular polarization of the observed wave.

varies from $V_{\rm trail}$ 200–220 km s^{-1}. The total duration of the satellite journey inside the structure is approximately equal to $\delta t \simeq 7$ minutes. Assuming that the component of the normal velocity along the satellite trajectory varies from 20 to 200 km s^{-1}, one can evaluate the total distance along the chord to be equal to

$$L \simeq \frac{(V_{\rm lead} + V_{\rm trail})}{2} t \simeq 5 \times 10^4 \text{ km}.$$

Figure 8 illustrates the geometry of the local configuration of the magnetic tube. A very important feature of our observations should be pointed out: the difference of the direction of the magnetic field before and after the structure. The magnetic fields before and after the structure make an angle of approximately 30° that corresponds to a rather important shear of the magnetic fields; thus, the structure as a whole represents the current sheet. We shall discuss it in Section 4 in more detail.

3.2. Event 2—Compressional Structure

This event was registered on November 4 from 17:05:34 to 17:06:50. Its crossing took a shorter time interval than previous structures. This structure represents another group of "switch-backs" that has different characteristics than the previous event. The major difference consists in quite a strong variation of the magnitude of the magnetic field inside the structure. On average, it is significantly smaller inside the structure than outside, and at the same time, the ion density according to ion distribution measurements by SWEAP decreases also. The ion temperature increases simultaneously with the decrease of magnetic-field magnitude. Moreover, the magnetic field undergoes quite strong variations inside the structure. The variations of the normal and radial components are up to tens of percent. According to these observations, namely, the correlation of the magnetic-field magnitude and density decreases, in terms of the MHD waves classification, the structure should have belonged to a fast magnetosonic mode rather than the Alfvénic wave mode. However, we shall demonstrate that there are some important characteristics that are similar to Alfvénic structures.

The basic plasma parameters for this structure are listed in Table 2.

Figure 9 represents the parameters of the structure: panel (a) shows the three components of the magnetic field. The structure starts with the sharp decrease of the magnetic-field magnitude from 70 to 30 nT and the simultaneous change of the radial component from about −70 nT to about −6 nT, followed by the partial rebound to about −45 nT and then the major jump to 52 nT. At the same time, the tangential component increases from about 10 to 60 nT, and the normal component changes its sign and jumps from −10 nT to about 40 nT. These variations happen in about 10 s intervals from 17:05:26 to 17:05:37. At 17:06:25, the magnetic field begins its return, and the major jump takes place from 17:06:26 to 17:06:36. An additional jump of the magnetic field occurs at about 17:06:46 when the magnitude of the radial component of the magnetic field decreases to negative values of several nT, and the total field becomes small of the same order, and, reaching a minimum, the field quickly returns to quasi-stationary outside values. Panel (b) shows the waveform of magnetic fluctuations recorded by the SCM instrument. They are very intense with the dominant component in the normal direction and amplitudes as large as several nT (up to 8 nT). The most intense oscillations are in the frequency range from 1 to 2 Hz to about 10 Hz. The bouncing of the DC magnetic field

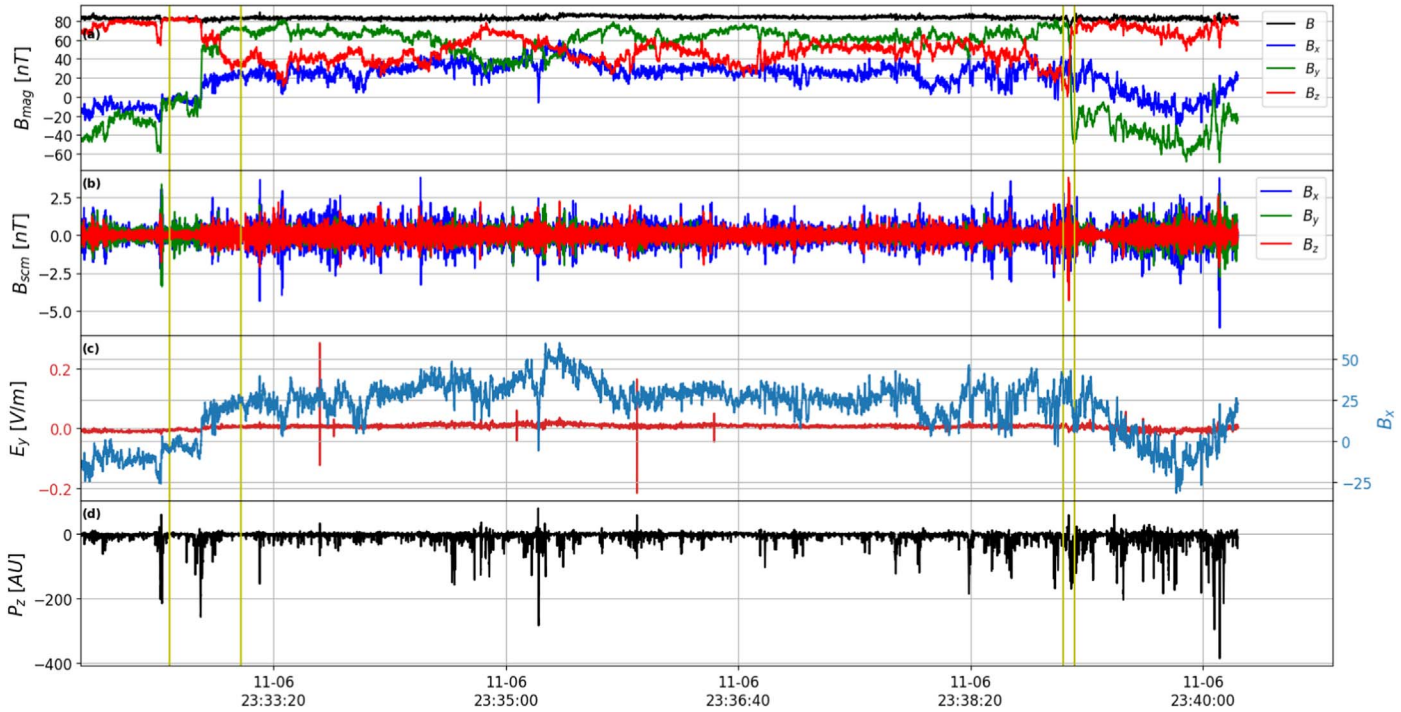

Figure 7. Poynting flux evaluation. Panel (a): magnetic-field measurements by the MAG instrument during the structure crossing in the satellite *xyz* reference frame. Since there are only two components of the electric field measured on board PSP *x* and *y*, for this particular Figure, the data is presented in the satellite reference frame, contrary to the other Figures. The components are colored *x* in blue, *y* in green, and *z* in red. Panel (b): magnetic-field fluctuations registered by the SCM instrument; colors are similar to panel (a). Panel (c): *y*-component of the electric field registered by the FIELDS suite is shown in red, and the *x*-component of the magnetic field by the MAG instrument is shown in blue. These field components are used together with the *x*-component of the electric field and the *y*-component of the magnetic field for the evaluation of the *z*-component of the Poynting flux. (d) *z*-component of the Poynting flux during the time interval including the Alfvénic structure crossing. The vertical lines mark the intervals around the structure's leading and trailing edges.

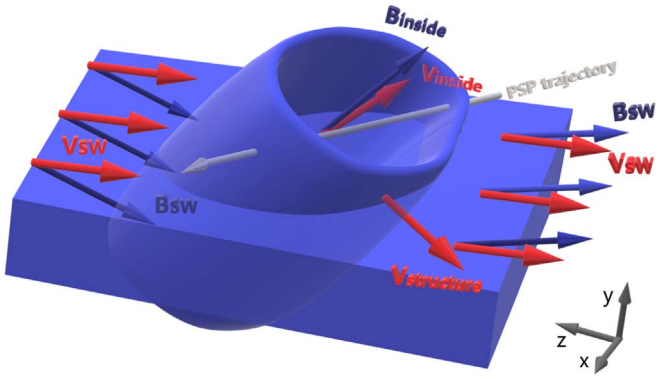

Figure 8. Schematic illustration of the magnetic structure shown in Figure 2. The solar-wind plasma bulk velocity is shown by the red vectors $\boldsymbol{V}_{\rm SW}$ (for the background solar wind) and $\boldsymbol{V}_{\rm inside}$ (inside the structure); the magnetic field is shown by the blue vectors $\boldsymbol{B}_{\rm SW}$ and $\boldsymbol{B}_{\rm inside}$, respectively. The solar-wind bulk flow velocity ahead and behind of the encounter is about the same while the magnetic field vectors have slightly different directions indicating the current system on the boundary of the structure. The velocity of the plasma flow inside the structure has two components: the flow along the field lines parallel to the tube axes $\boldsymbol{V}_{\rm inside}$ (along the magnetic field in the structure), and as the component related to the structure motion $\boldsymbol{V}_{\rm structure}$. Thus, the total bulk flow velocity of the plasma inside the structure is $\boldsymbol{V}_{\rm flow} = \boldsymbol{V}_{\rm inside} + \boldsymbol{V}_{\rm structure}$. The gray line illustrates the trajectory of the satellite crossing the structure.

just before and a little after encounter is filled in by very intense magnetic oscillations. Panel (c) shows the spectra of the magnetic fluctuations obtained from the SCM instrument measurements. The magnetic fluctuations frequency range goes up to 100 Hz. The wave activity is quite intense around both the boundaries. Panel (d) shows the electron density estimated by means of the QTN technique. In our study, we use density, bulk flow, and thermal velocity measured by the SWEAP instrument as they are better adapted for the studies of sharp boundaries. Panel (e) provides an evaluation of the thermal velocity of ions, and the strong increase of it inside the structure results in a strong growth of the plasma ion beta from $\beta \simeq 0.55$ outside the structure to $\beta \simeq 1.8$ inside and then rebounds to 0.49 after encounter. A possible role of the sharp ion plasma beta variations for the equilibrium of the structure will be discussed later. It is worth noting that the dominant parameter in comparison with the pressure balance remains the dynamic pressure of the plasma flow. Another important feature is the density enhancement on the leading and trailing edge (which begins inside the structure), presumably related to the plasma drag on the boundaries.

The variations of the magnetic field and velocity around the leading edge of the structure are presented in Figure 10. Panel (a) shows the variations of the magnetic field as registered by the MAG instrument in the RTN frame. Panel (b) represents the variations of the magnetic field components across the boundary corresponding to the largest (blue), intermediate (green), and the smallest (red) eigenvalues. In order to complete this analysis, the MAG data was filtered to remove the fields in the frequency range higher than 0.2 Hz. The ratio of the second to third eigenvalues is about two, which indicates rather large error bars caused by the wave activity around the boundary. The normal unit vector to the boundary $N_{\rm lead} = [-0.33;\ 0.07;\ 0.94]$ is close to the normal northward direction with a small radial component. The normal to the boundary component of the magnetic field is rather large $B_n = 24.4 \pm 5.9$ nT. Panel (c) shows that variations of the velocity vector are synchronous with the magnetic field.

Table 2
Basic Plasma Parameters for Compressional Structure

Parameter	Before Encounter	Inside Structure	After Encounter
Magnetic-field Vector (nT)	[−68.6;16.6;−1.6]	[26.9;42.3;21.7]	[−65.5;−13.1;8.5]
Magnetic-field Magnitude (nT)	70.6	54.6	67.3
Velocity Vector (km s^{-1})	[301.3;42.8;15.7]	[402.0;68.3;27.1]	[293.4;16.1;28.9]
Velocity Magnitude (km s^{-1})	304.8	408.6	295.2
Ion Plasma Density (cm^{-3})	311	282	302
Ion Temperature (eV)	21.5	46.5	18.3
Ion Beta	0.54	1.8	0.49
Ion Inertial Length c/ω_{pi} km	12.9	13.6	13.1
Ion Larmor Radius V_{Ti}/Ω_i km	6.6	12.5	6.4

Panel (d) shows variations of the component of the velocity along the normal to the boundary direction; it varies in the range 85–105 km s^{-1}. It was found to be slightly different to the magnetic field defined: the difference is 19°. Figure 11 shows the waveform of the magnetic field components registered around the leading edge of the structure by SCM filtered in the frequency range of 2–5 Hz. The wave *k*-vector was found at 60° with respect to the normal to the boundary. This indicates that the wave can be considered a surface wave (Hollweg 1982). The wave frequency is rather close to the local ion cyclotron frequency.

Figure 12 shows variations of the magnetic field and velocity vectors around the trailing-edge boundary. The magnetic field (panel (a)) returns to the parameters rather close to those before the encounter, the radial component becomes dominant, and the normal and tangential become relatively small. Panel (b) shows variations of the magnetic field in the MVA reference frame with the same colors as for the leading edge. Variations of the velocity vectors (radial is shifted down to 300 km s^{-1}) are presented in panel (c), and panel (d) shows variations of the normal to the boundary component of the velocity varying in the range 40–60 km s^{-1}. However, one should note that there is the important difference of magnetic-field directions before and after the encounter: the significant tangential component of the field while the normal component was sufficiently smaller, and after the tangential component became practically negligible, whereas the normal component became rather significant. The angle between magnetic field vectors before and after encounter is approximately 27°, the angle between velocity vectors is much smaller—about 5°.7. One can conclude that the structure carries some integral current that results in important shear of the magnetic field. In Figure 9, the presence of the quite intense wave activity around both leading and trailing edges of the structure was evidenced. The waveform and its hodograph of the wave around the trailing edge are presented in Figure 13. It is worth noting that the angle between *k*-vector of the wave and the normal to the surface makes 60°.5. It supports the assumption that this wave is the surface wave. It is worth mentioning that there may exist different types of wave activity around the boundary of compressional structure, namely, whistler waves, as it was reported by Agapitov et al. (2020). We present wave characteristics for the trailing edge in more detail in Figure 15. Panel (a) shows the waveform of the three components of the magnetic field fluctuations obtained in the frequency range 2–5 Hz. In panel (b), we show the hodograph of two largest components of the wave magnetic field that indicate the wave is close to the circular polarization. The angle between the wave *k*-vector and the normal to the boundary is found to be about 80°, so, the wave can be considered a surface wave.

One of the characteristics used to classify the discontinuities in the solar wind is Alfvénicity. It is manifested in the absence of variations of the magnetic-field magnitude and in synchronous variations of the velocity and magnetic field perturbations related linearly as described in previous paragraph. We have already mentioned that the magnitude of the magnetic field manifests very important variations. This indicates that the structure may not be considered purely Alfvénic. Correlation between the decrease of the magnetic-field magnitude and ion density provides a strong argument in favor of attribution of this structure to fast magnetosonic mode. The results of the check of another condition, the linear correlation between perturbations of the magnetic field and velocity vectors, are presented in Figure 14. It shows the variations of the radial component of the magnetic field and of the radial velocity, which undergo the largest changes. On the leading edge of the boundary, one can conclude that the correlation is quite convincing, and it is similar to that observed for the Alfvénic structure. However, there is an important difference of the coefficients of linear relation between the leading and trailing edges that might arise from the significant change of the plasma parameters between the two boundaries. To outline the similarity and differences, the average values evaluated before the structure were subtracted. The linear correlation is good for the leading-edge transition, except for the region where the local density strongly increases, but the fitting of the trailing-edge boundary shows a significant difference. The normal unit vector to the trailing-edge boundary $\boldsymbol{n}_{\rm tr} = [0.18; -0.59; 0.78]$. The component of the magnetic field orthogonal to the boundary is very close to zero, $B_n = 0.0 \pm 1.2$ nT. The wave activity of the surface waves around the leading and trailing edges may be characterized by means of an evaluation of the Poynting flux in the reference frame of plasma inside the tube. The data of the measurements of the fields and velocities allow one to to evaluate the *z*-component of the Poynting flux (it is close to the radial direction). In order to do so, as in the previous case, the *x* and *y* components of the electric and magnetic fields are used in the satellite reference frame. The VxB electric field is evaluated and removed from the data, and the Poynting flux is estimated. The results are presented in Figure 15. Panel (a) shows the magnetic field, panel (b) shows the SCM waveforms, and panel (c) shows the Poynting flux. The Poynting flux enhancement is observed around both the leading and trailing edges of the structure, and the Poynting flux is negative, which corresponds to the direction away from the Sun.

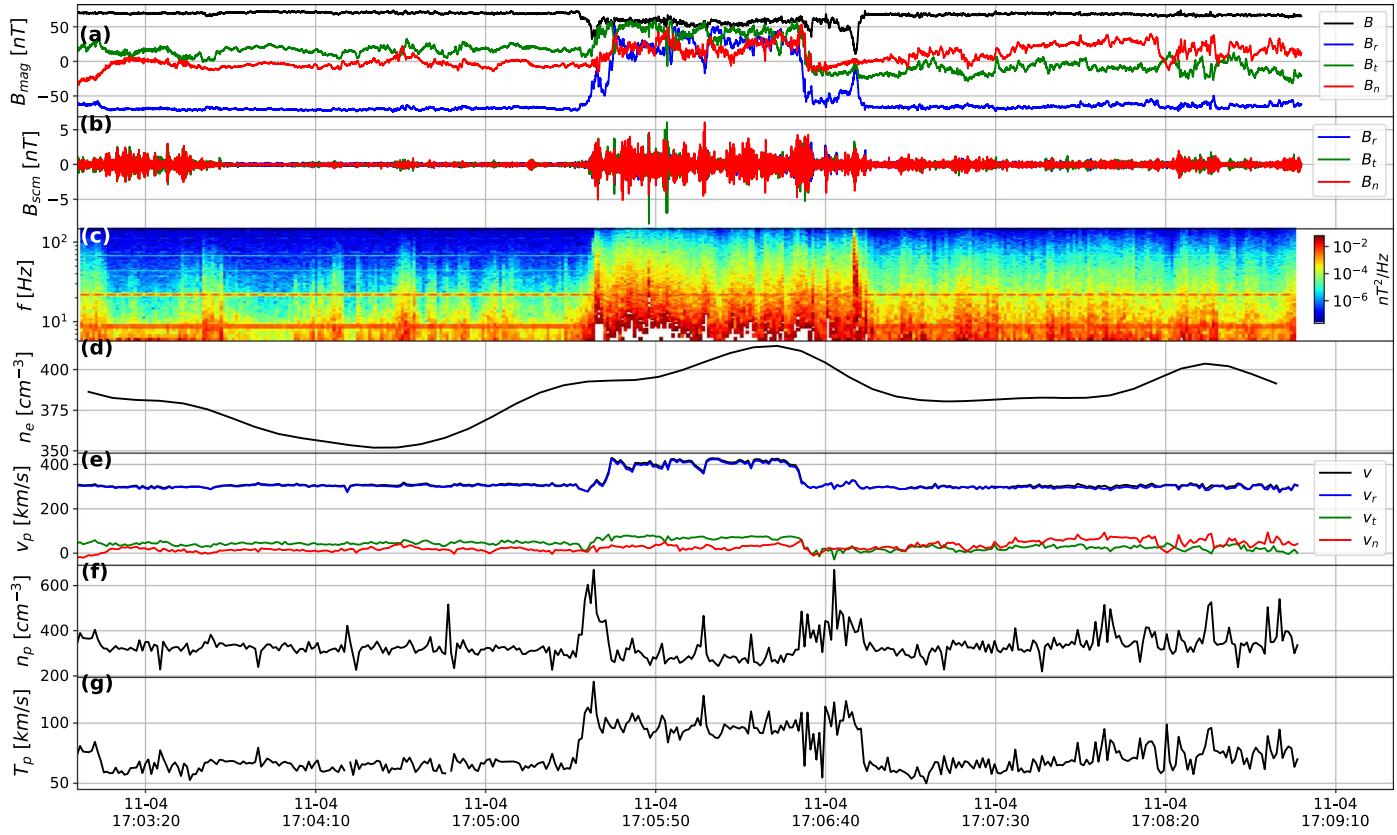

Figure 9. Compressional magnetic structure is in the same format as in Figure 2.

The characteristic spatial variations of the system around and inside the structure, similarly to the previous case, are much larger than characteristic scales in plasma, the Larmor radius, and ion inertial scale; thus, the analysis of plasma flow motions necessitates a similar approach. One can separate the total motion from the flow motion along the magnetic-field lines and orthogonal magnetic-field-line motion of the magnetic-field tubes. Applying similar procedures, one can find the velocity parallel to the magnetic field before encounter to be equal to 282.8 $\mathrm{km\,s^{-1}}$, and the magnetic-field tubes' relative velocity perpendicular to their direction $\boldsymbol{V}_{\perp/\mathrm{bef}} = [127.7; 133.3; 21.4]$, $|V_{\perp/\mathrm{bef}}| = 185.8\ \mathrm{km\,s^{-1}}$; here, the index $\perp/\mathrm{bef}$ signifies the perpendicular to the magnetic-field-direction component of the velocity of plasma before the structure. Supposing that the satellite crosses a tube-like structure, we assume that it is much longer along its axes than in perpendicular directions. For the sake of simplicity, it may be considered as having a cylindrical cross section. Under such assumptions, one can find that the flow velocity along the magnetic field is equal to $|V_{\mathrm{par/in}}| = 260.4\,\mathrm{km\,s^{-1}}$, and the orthogonal velocity of the tube may be estimated to be equal to $\boldsymbol{V}_{\perp/\mathrm{in}} = [274.4; -132.2; -77.2]$, and $|V_{\perp\mathrm{in}}| = 314.2\,\mathrm{km\,s^{-1}}$. The angle between average magnetic fields inside the structure and outside before the encounter is 72°.2. Taking estimates of the normal to the boundary component of the velocity at the leading and trailing edges of the structure, one can evaluate the length of the chord corresponding to path of the satellite as $L \simeq \frac{1}{2}(V_{n/\mathrm{lead}} + V_{n/\mathrm{out}})\delta t = 7000\,\mathrm{km}$. The evaluation of the angle between the tube velocity and the normal to the structure shows that the satellite enters inside the cylinder where the velocity vector makes an angle with the normal to the cylinder of approximately 56° and quits it with the angle 78°. These estimates are rather rough, but they provide an idea that the crossing chord is of the order of the diameter of the tube; thus, the estimate of the scale above gives a reasonable size of it. It is worth noting, as in the previous case, that the structure supposedly carries some integral current resulting in significant shear of the magnetic field, and the fields before and after it make an angle of 27°.

3.3. Event 3—Switchback with Full Reversal of the Magnetic Field

The satellite crossed the structure at November 5 from 04:27:40 UT to 04:42:05. The basic parameters of the plasma during this encounter are presented in Table 3.

The plasma moments by the SWEAP instrument are rather poor for this time interval. The only plasma parameter available for this event is an electron density estimated from the Quasi-Thermal Noise (QTN) technique. It varies between 460 and 530 $\mathrm{cm^{-3}}$ inside the structure.

Figure 16 represents variations of the magnetic field, spectra of magnetic fluctuations, and an electron density profile evaluated making use of the QTN technique during the crossing of the magnetic structure with the reversal of the radial component of the magnetic field. The switchback here consists of the reversal of the radial component of the magnetic field and its return. It begins at 04: 27: 40, when the sharp change of the radial component of the magnetic field occurs. It results in a drastic change of the field magnitude from −58 to 26 Hz. This transition happens in about 10 s time intervals. The radial component of the field remains large and positive until 04: 36: 35, when it begins to return to negative values and reaches a value of about −60 Hz for a short time interval. After

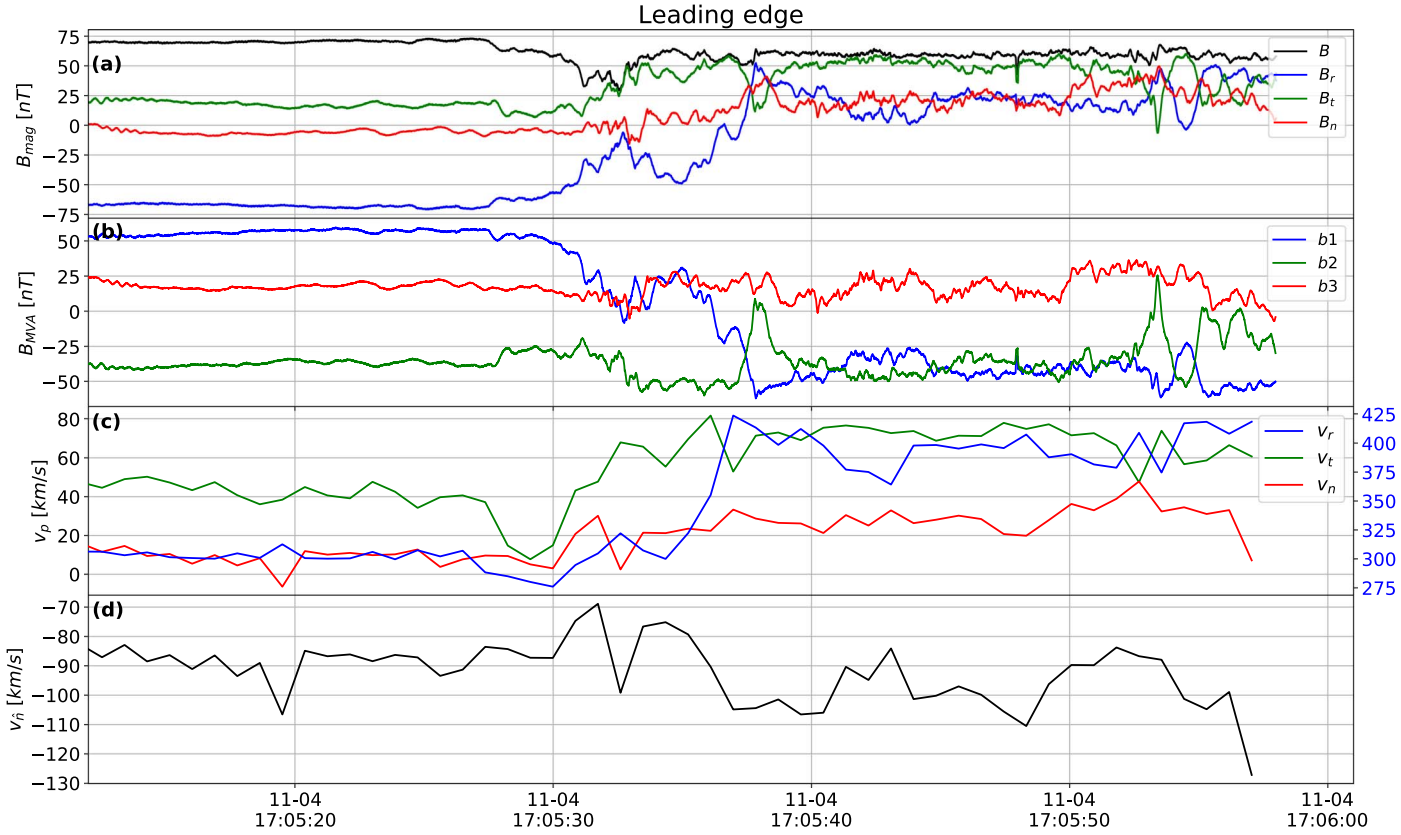

Figure 10. Magnetic field and plasma bulk flow velocity on the leading edge of the compressional structure shown in Figure 9.

that, it increases again to positive but smaller values from 0 to 45 Hz, and during the time interval 04: 42: 00 to 04: 42: 05, it returns to large negative values, even larger than before the encounter, of about 70–75 Hz. The second panel (b) represents the waveform of the magnetic field fluctuations measured with the SCM instrument, and panel (c) represents the power spectral density of the magnetic field fluctuations evaluated using the SCM instrument. There are many spikes of high intensity in the frequency range from 5.7 Hz to several tens of Hz. Panel (d) shows an electron density profile obtained from electric-field measurements making use of the QTN technique (Moncuquet et al. 2020). The profile presented is smoothed and cannot correctly represent the sharp boundaries. Large-scale density variations are of the order of 40 cm^{-3}, which is of the order of 10%.

In order to characterize the boundaries, we carried out the MVA analysis again. The normal vector to the leading edge is $\boldsymbol{N} = [-0.12;\ 0.21;\ 0.97]$. It is very close to the normal direction perpendicular to the equatorial plane. It is worth noting that in addition to the major variation of the radial component, there is a small but significant variation of the tangential component from about 35–70 nT. In order to illustrate the field dynamics across the boundary, we present in Figure 17 a more detailed view of the time variation of the magnetic field around the leading and trailing edges. The low-pass filtered (<0.2 Hz) components of the magnetic field are presented in panel (a) of Figure 17. The magnetic field has a significant component along the normal to the boundary of the leading edge $B_N = -43.9 \pm 5.3$ nT. Time variations of the magnetic-field components in the MVA reference frame are shown in panel (b) of the same Figure. In the panels presenting the results of the MVA analysis, we use the same colors as for previous events. A similar analysis applied to the trailing-edge boundary shows that the normal vector to it $\boldsymbol{N} = (0.38, 0.65, -0.66)$ is mainly in the normal-tangential plane with a small radial component, and it makes an elevation angle in the plane close to 45°. The normal component of the magnetic field on this boundary is sufficiently smaller than at the leading edge: it is equal to $B_N = -13.3 \pm 5.8$ nT. It is worth noting that several of the structures we analyzed have large normal components of the magnetic field on one boundary and relatively small components on the other. The magnetic-field variations for the trailing edge are shown in panel (c) of the same Figure 17, and the variations of the eigenvectors corresponding to largest, intermediate, and smallest eigenvalues of the field are shown in panel (d). One of the important characteristic features used for the determination of the property of so-called "Alfvénicity" over the discontinuities consists in the absence of the variation of the magnetic-field magnitude while the components vary across the boundary. Considering the whole structure, one can observe quite important variations of the magnitude of the magnetic field; however, at the leading-edge transition, there is not any significant variation of the magnitude of the magnetic field. The trailing-edge transition may be "non-Alfvénic," and the magnitude of the field undergoes quite an important jump from about 65 nT to approximately 80 nT. One important observation to be pointed out emerges from the evaluation of the angle between the magnetic field before the structure and after its crossing: the angle it makes is 35°. This leads to the suggestion that the currents flowing on the surfaces of the leading and trailing edges result in the significant shear of the surrounding magnetic field. Another important feature of the structures observed is the high intensity of the wave activity in

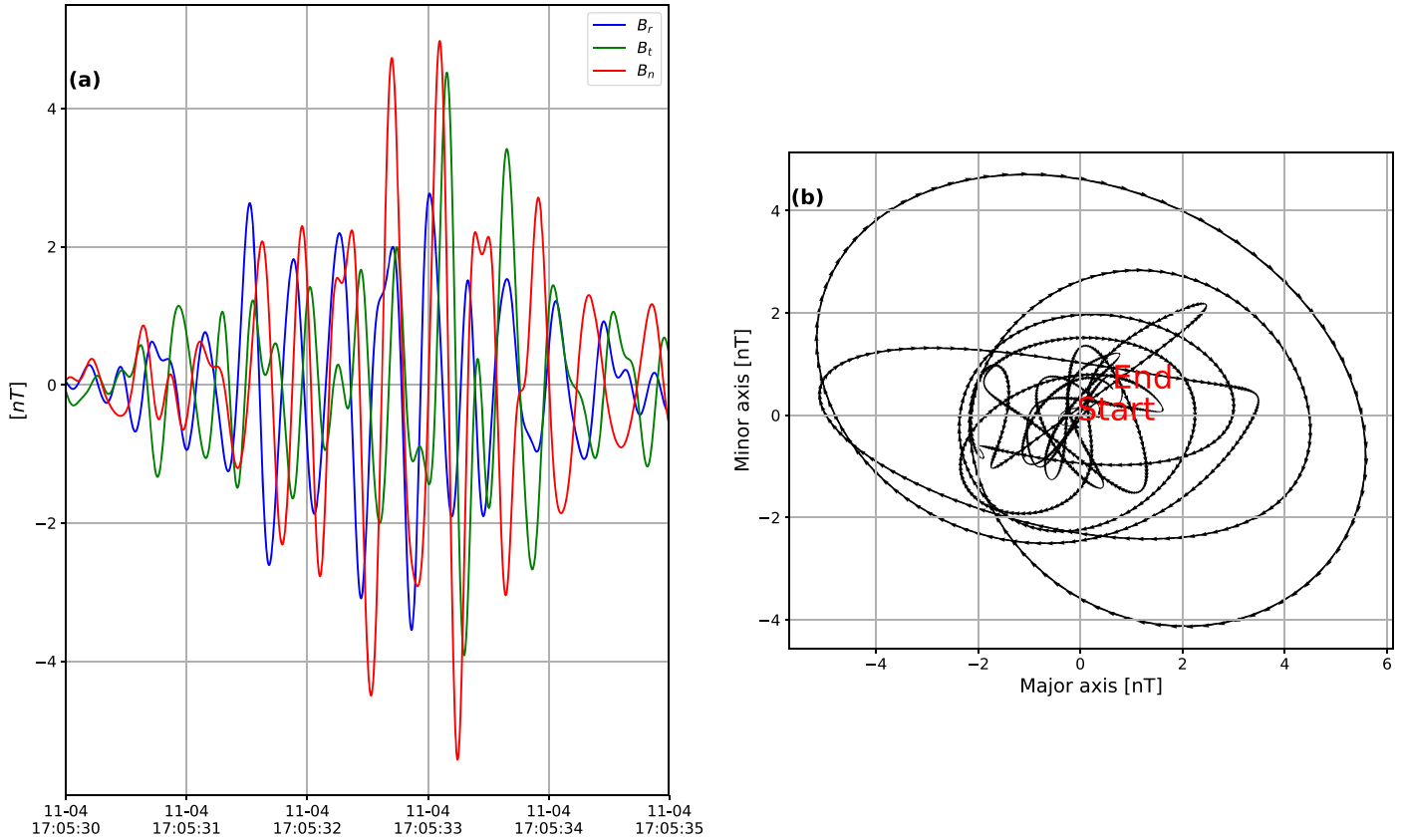

Figure 11. (a) Waveforms of the magnetic-field components in the RTN frame recorded in close vicinity to the leading edge of the structure shown in Figure 9. (b) Hodograph of the magnetic field in the plane transverse to the wave normal vector.

the frequency range from 5.7 Hz (low limit for the spectra we adopted) to several tens of Hz, manifested in the spectra of the SCM typically more than an order of magnitude higher than in the surrounding quiet plasma flow, as it was also pointed out by Dudok de Wit et al. (2020). Unfortunately, our analysis for this particular event is limited by FIELDS instruments measurements only; SWEAP data for it contain poor-quality data sets and are not usable for the detailed analysis.

4. Interpretation of Observations and Discussion

Our data analysis may be summarized as follows. The structures we observe are large in comparison to the typical characteristic scales in plasma, such as the Debye length, the ion and electron Larmor radii, and the ion and electron inertial lengths, except for their boundaries. One of the boundaries is of the order of several ion inertial lengths or ion Larmor radii (they are of the same order of magnitude). Time variations of macroscopic motions of plasma are also slow with respect to the ion gyroperiod, which is the largest characteristic timescale of particle motions. The only exception is the wave activity in the vicinity of the boundaries, which we shall discuss later. We examined the properties of three selected structures that we consider as representatives of three different groups: (a) Alfvénic-type structures where magnetic-field variations occur without a change of the magnitude of the magnetic field, (b) compressional-type structures where the magnetic-field magnitude varies and is accompanied by/associated with the variations of the plasma density, and (c) full reversal of the radial component of the magnetic field, but similar to the Alfvénic-type structure. To determine the "local design" of the structures, we carried out an analysis of the plasma motions and fields inside and around the structures with special attention to their boundaries. Since the plasma is fully ionized, collisionless and characteristic scales of spatial variations are large, so one can treat its macroscopic motions as "frozen in," except its boundaries. This suggests the separation of its motion into two parts: the flow motion of the plasma that is directed along the magnetic field, and the motion of the magnetic field tubes in the direction perpendicular to their axes. Plasma characteristics inside and outside the structures are found to be rather different, and there are several parameters making this difference. They are: the direction of the magnetic field, the plasma density, the flow velocity and ion beta, and the ratio of the ion thermal pressure to the magnetic pressure, which was found to be larger than one inside the structures and significantly smaller outside. The magnetic field before the structure and after it manifests significant change. The angles between the fields before and after are larger than 25° (we show it for our selected examples, but we checked it for about 20 other events), which results in a magnetic field difference of the order of 30 nT; thus, the structures themselves may be considered the system of current sheets that carries some total current. This change is sufficiently smaller than the difference of fields inside and outside the structure, but it should not be neglected. In order to characterize the parameters and geometry of the structures, we performed an MVA analysis of the magnetic-field variations of the boundary current sheets and determined their characteristics (it was done for about 20 other structures, but the statistical study will be presented in a separate publication). This analysis allows one to estimate the magnetic-field jump and the characteristic direction and the scale of the magnetic field change through

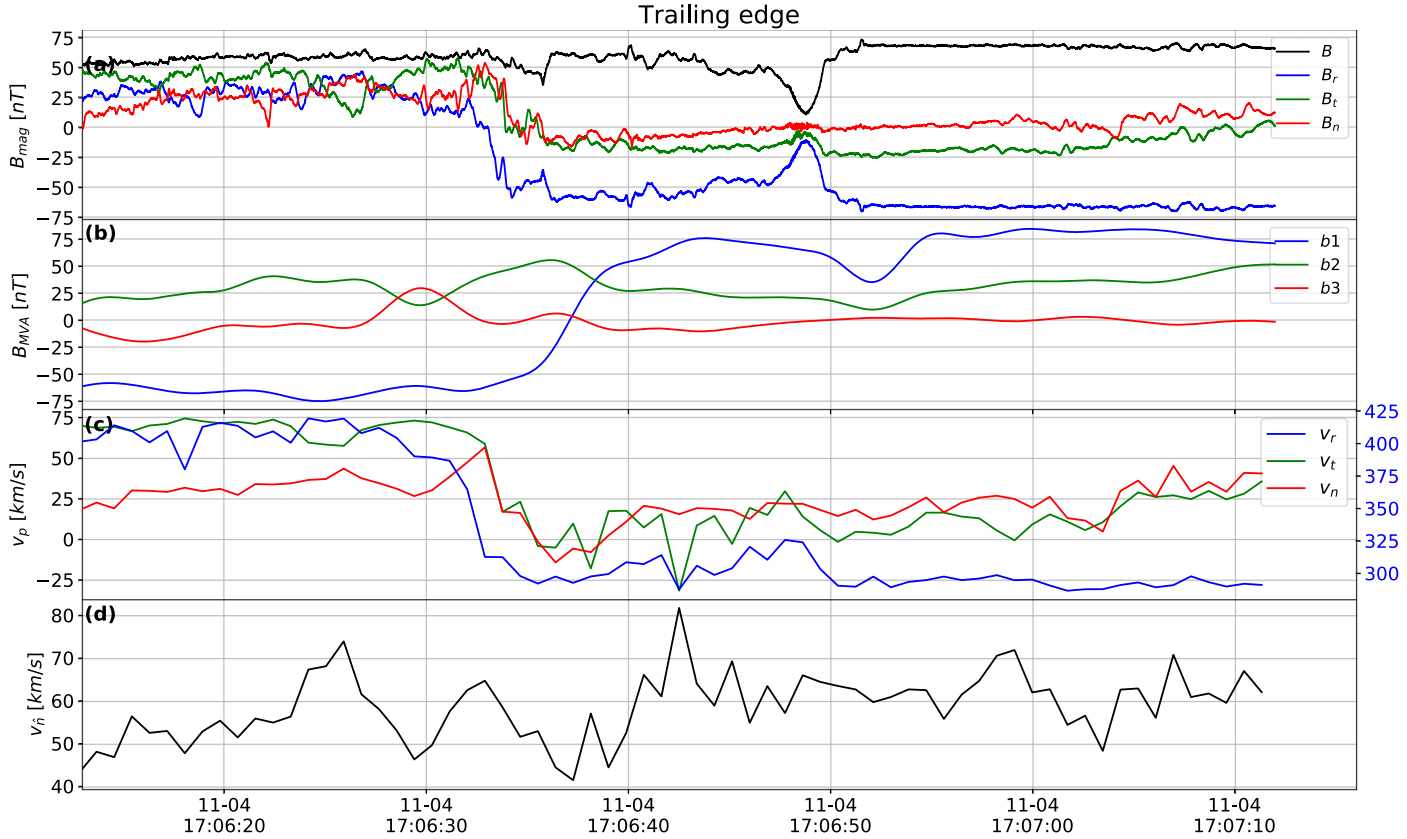

Figure 12. Magnetic field and plasma bulk flow velocity on the trailing edge of the structure shown in Figure 9.

the boundaries. Now, we shall use these characteristics to evaluate the distribution of currents across the boundaries. The knowledge of the direction of the magnetic field inside the tube that coincides with its axes allows us also to separate the current observed on both the leading and trailing edges of the structure onto tube-aligned and azimuthal. The azimuthal current provides a diamagnetic effect that compensates for the magnetic-field difference along the tube axes inside and outside. The tube-aligned current in its turn flows on both sides of the tube surface in opposite directions and may lead to the shear of the magnetic field outside the structure. Our analysis reveals the following characteristics for the three structures we presented.

4.1. Alfvénic Structure

The leading edge of the structure, more precisely, the major jump of the field (it may be called ramp similarly to shocks), was crossed on November 6 from 23:32:48.4 to 23:32:49.6, i.e., the duration of crossing is approximately 1.2 sec (see details in Figure 5, panels (a) and (b)). The jump of the magnetic field during the ramp crossing was about 75 nT, but there was an additional smaller jump at 23:32:56.8, of the duration of 0.6 s, and only then was the final value of the field inside the tube achieved. For the sake of simplicity of estimate, we shall take it as one single jump from the outside to inside value of the field of the duration of 1.8 s. The average normal velocity during this period was about 25 $\mathrm{km\,s^{-1}}$ (panel (d) of Figure 5); thus, the characteristic spatial scale of the layer is about $\delta L \simeq 45$ km. In order to evaluate the average magnetic field before the encounter, we choose an interval from 23:29:10 to 23:30:49 when the variations of the field components are relatively small (less than 10 %), and we filter the data, keeping only frequencies less than 1 Hz. Then, we calculate an average magnetic field on this interval before encounter outside the structure. To evaluate the average magnetic field inside the structure, we take an interval from 23:33:51 to 23:38:12 that is slightly distant from both boundaries and proceeds in a similar way. We proceed in the same way to compute the average field after the encounter in the interval 23:40:20–23:42:56. The average magnetic field vector outside before the encounter is $<\boldsymbol{B}_{\rm before}> = [-75.\ 8; -17.5;\ 22.5]$ nT, and inside $<\boldsymbol{B}_{\rm inside}> = [-46.\ 1;\ 27.5; -63.6]$ nT. This results in a total jump of the magnetic field vector $<\delta\boldsymbol{B}> = [29.\ 7;\ 45.0; -86.1]$, with magnitude $|\delta B| = 101.6$ nT. It is worth noting that the angle between the normal to the boundary and upstream magnetic field before encounter makes 82°. The normal component of the magnetic field is found to be $B_n = -2.5 \pm 3.2$ nT, which makes it reasonable to speak about the quasi-perpendicular boundary layer or in terms of discontinuities TD. The evaluation of the current density results in $j \simeq \frac{\delta B}{\mu_0 \delta L} \simeq 1800\ \mathrm{nA\ m^{-2}}$. The current flows along the narrow surface of the tube. Its thickness is of the order of 4–5 ion Larmor radii. The current makes an angle of 23° with the direction of the magnetic field outside the tube and an angle of 30° with the axes of the magnetic tube. Thus, the current density along the tube axes, which we might call the tube-aligned current density, is approximately $j_{\rm par} \simeq 1530\ \mathrm{nA\ m^{-2}}$, and the azimuthal component $j_{\rm az} \simeq 950\ \mathrm{nA\ m^{-2}}$. The difference of the magnetic field between the two sides of the structure is significantly smaller than the difference between the field inside and outside of the structure. It justifies a suggestion that in a first-order approximation, the current closure occurs on

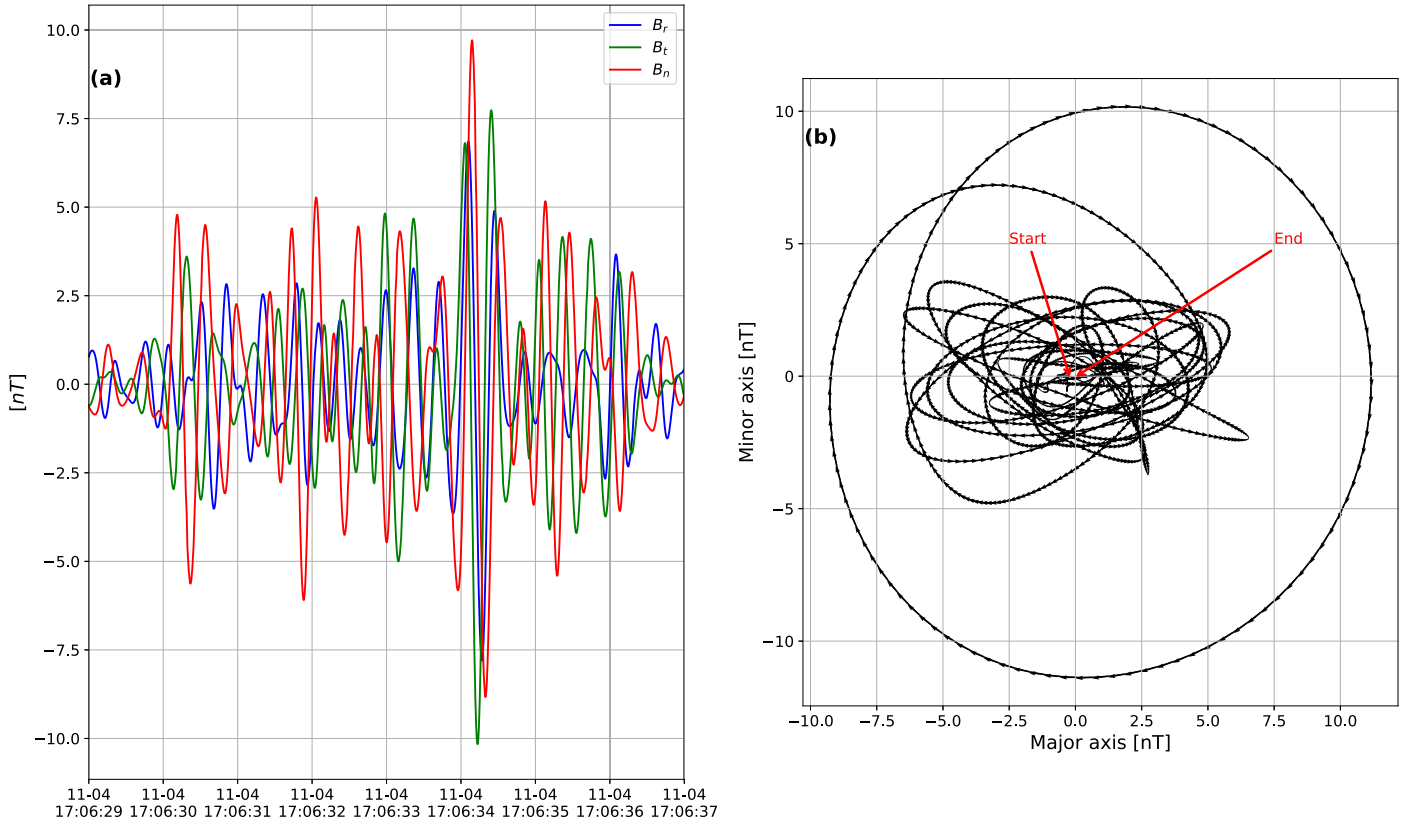

Figure 13. (a) Waveforms of the magnetic-field components in the RTN frame recorded in close vicinity to the trailing edge of the structure shown in Figure 9. (b) Hodograph of the magnetic field in the plane transverse to the wave normal vector.

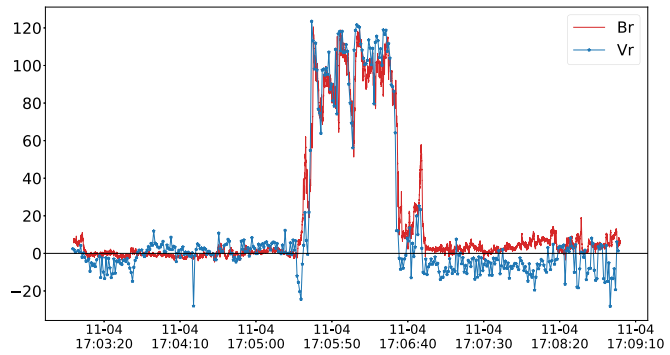

Figure 14. Radial components of the magnetic field (red) and plasma bulk velocity (blue) during the crossing of the structure (Figure 9), illustrating close to the linear correlation, i.e., a high level of Alfvénicity. The Alfvénic type of perturbations is on the leading edge; however, the change of components around trailing edge is presumably due to the change of plasma parameters across the structure. The *y*-scale is the same because the respective mean computed over the data prior to encounter (17:03–17:05:26) has been subtracted.

the same surface of the tube. Surprisingly, the tube-aligned component of the current is significantly larger than azimuthal component, which signifies that the current circuit element should be placed on a very oblique ellipsoid. This is easy to understand, because this current should provide the magnetic field equal to the difference of the magnetic field inside and outside of the structure. If we consider that this structure could be produced by the current loop, it should flow in the plane perpendicular to the vector equal to the difference of the two magnetic field vectors. The trailing-edge crossing time is also about two seconds from 23:39:02 to 23:39:04, but the normal component of the velocity is about 220 km s^{-1}, as one can see on Figure 6, almost 10 times higher than that for leading edge. Thus, the thickness of the trailing-edge current sheet is also about 10 times larger, about 440 km. Its width is sufficiently larger than any characteristic scale of the plasma. The boundary is significantly broader and more diffuse, but the thickness of the layer remains much smaller than the size of the structure. The difference of the average magnetic field after the encounter and inside the structure is

$$\delta \boldsymbol{B} = [28.3;\ 8.7;\ 86.6]\ \text{nT},\ |\delta B| = 91.5\ \text{nT}.$$

The current density may be evaluated to be

$$\frac{\delta B}{\mu_0 \delta L} \simeq 165\ \text{nA m}^{-2}.$$

It is an order of magnitude smaller than the one at the leading edge. The current has a direction almost opposite to the current on the surface of the leading edge; the angle between the direction of the tube axes and the direction of the current makes 33°, and the tube-aligned and azimuthal components of the current density have magnitudes as follows:

$$j_{\text{par}} = 139\ \text{nA m}^{-2};\ j_{\text{az}} = 89\ \text{nA m}^{-2}.$$

The cut of the tube corresponding to the surface where the current flows will present an ellipsoid that is very oblique with respect to the tube axes; the angle that the largest axes of the ellipsoid makes with the tube axes is about 33°. A sketch that shows such a current element is presented in Figure 18.

It is worth noting that the angle between the direction of the current flow and an average magnetic field after encounter

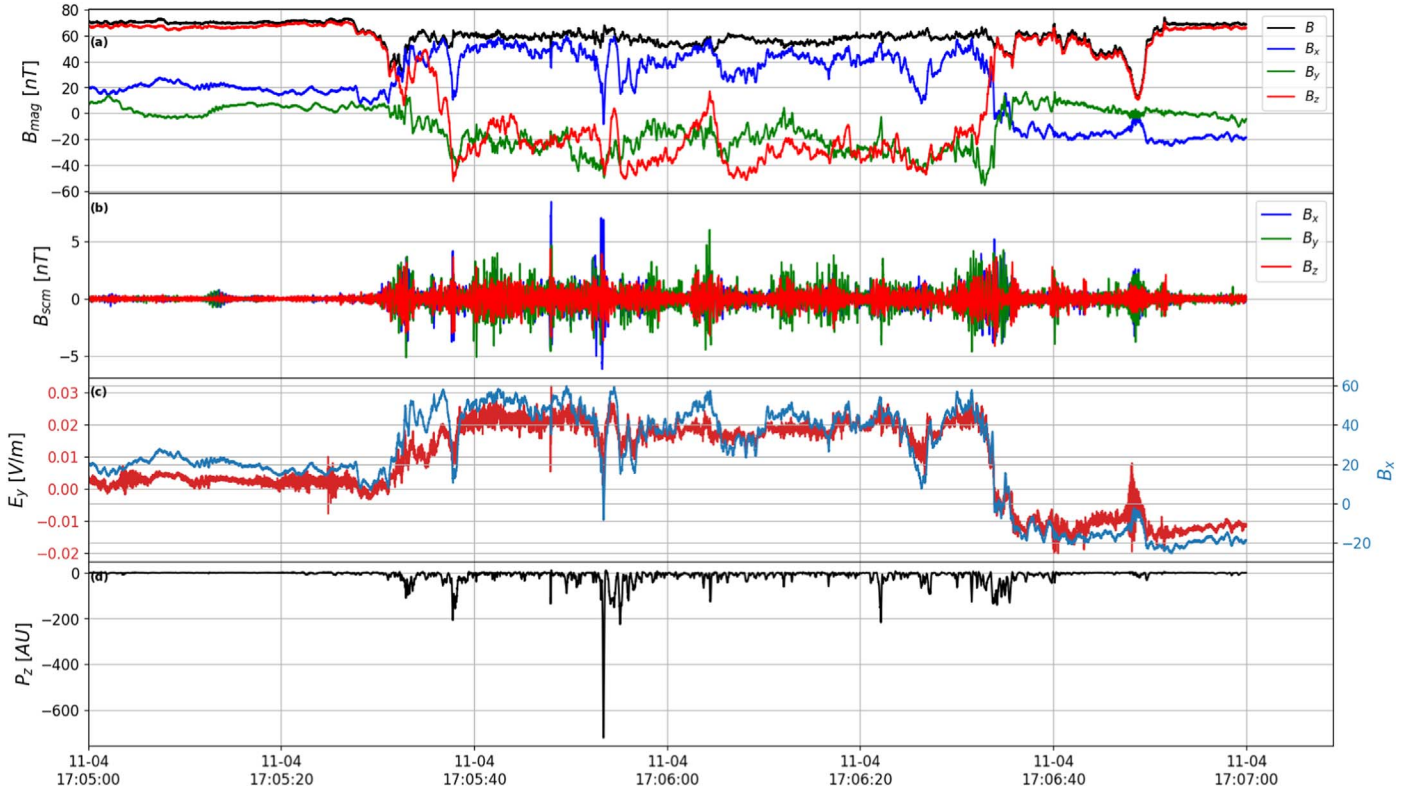

Figure 15. Poynting flux evaluation for compressional structure. Panel (a): magnetic-field measurements by MAG instrument during the structure crossing in satellite *xyz* reference frame; similarly to Figure 7, the data are presented in the satellite reference frame. The components are colored *x* in blue, *y* in green, and *z* in red. Panel (b): the magnetic-field fluctuations registered by the SCM instrument; the colors are similar to those in panel (a). Panel (c): the *y*-component of the electric field registered by the FIELDS suite is shown in red, and the *x*-component of the magnetic field by the MAG instrument is shown in blue. The correlation between variations of components is related to the important electric-field-induced due $\boldsymbol{V} \times \boldsymbol{B}$ plasma motion. These field components are used together with the *x*-component of the electric field and the *y*-component of the magnetic field for the evaluation of the *z*-component of the Poynting flux. Panel (d): *z*-component of the Poynting flux during the time interval including compressional structure crossing. Quite large fluxes directed along the *z*-axis are registered. It is worth reminding the reader that the *z* axis is quite close to the radial direction, and the negative flux is directed outward from the Sun.

makes 34°. An important feature of the system to be mentioned is that the magnetic fields before and after the encounter make an angle of 30°, which results in a difference of the fields $\boldsymbol{\Delta B} = [1.35; 36.3; 0.5]$ nT. Its magnitude is almost the same as the tangential component, as the vector is directed almost exactly in the tangential direction. It signifies that the structure itself represents a global current sheet. The precision of our measurements does not allow us to correctly evaluate its detailed characteristics. However, an interesting estimate about the direction of the global magnetic field may be found from the relative directions of the vectors of $\Delta \boldsymbol{B}$ and the axes of the magnetic tube. One can infer that the global current should flow under a very small angle to the axes of the tube of 17°. The currents at the leading and trailing edges need an application of some electric field. As is known (Braginskii 1965), the role of the "effective electric field" may play the gradient of the ion temperature and ion pressure. As was shown in Figure 4, both gradients are present and quite large. For the narrow current sheet at the leading edge, the current may be associated with the difference of ion and electron dynamics due to the relatively small scale of the layer in comparison with the ion Larmor radius being just several times larger it. On the other hand, for the thick layer observed at the trailing edge, the current may be determined by the presence of some anomalous collisions due to the wave activity. As was shown in Figure 6, there is intense wave activity at this boundary due to the presence of the surface wave having an angle with the boundary normal of 60.°5. The wave may affect magnetic-field motions of electrons in a parallel manner, as the field-aligned currents are carried preferably by electrons. It may also lead to an important energy and impulse exchange between ions having different energies resulting in azimuthal deviations of ion trajectories to provide important ion currents orthogonal to magnetic field lines. The wave electromagnetic field has a smaller scale than the boundary layer that may make the boundary surface rippled. The wave activity may also significantly enhance the diffusion processes through the boundary, which will lead to its widening.

4.2. Compressional Structure

This structure was traversed during a significantly shorter time period, and our estimate above showed that its characteristic cross scale of the tube is about 7000 km. The leading edge of it was crossed in the time interval from 17:05:26 to 17:05:37, which took 11 s with a rather high normal velocity about 90 km s^{-1}. Thus, the thickness of the current sheet layer is quite large, about 1000 km, and so, it is not really a sharp boundary but is rather diffuse. In terms of the relative angle between the upstream magnetic field and the normal to the boundary that the angle makes 71.°6, the transition remains quasi-perpendicular, but the relative velocity of the incoming flow is smaller than the fast magnetosonic speed; thus, the effect of the "shocking" of the flow consists only of the local increase of the plasma density but not on the

Table 3
Major Plasma Parameters for the Radial Component Reversal Structure

Parameter	Before Encounter	Inside Structure	After Encounter
Magnetic-field Vector (nT)	$\boldsymbol{B}_{\rm bef} = [-69.4; -9.7; -17.7]$	$\boldsymbol{B}_{\rm in} = [53.6; 51.2; 19.6]$	$\boldsymbol{B}_{\rm after} = [-72.4; 13.9; 20.2]$
Magnetic-field Magnitude (nT)	$\lvert\boldsymbol{B}_{\rm bef}\rvert = 72.2$ nT	$\lvert\boldsymbol{B}_{\rm in}\rvert = 76.7$ nT	$\lvert\boldsymbol{B}_{\rm after}\rvert = 76.4$ nT

scale of the current sheet. The normal component of the magnetic field is evaluated to be 24.8 nT; thus, the discontinuity is in between the TD and/or RD. The total jump of the magnetic field between the average upstream flow and the average flow inside the tube is expressed as a vector $\delta\boldsymbol{B} = [95.43; 25.71; 23.24]$ nT, and its magnitude is 101.5 nT. The current density inside the layer may be evaluated as

$$j \simeq \frac{\delta B}{\mu_0 L} = 115 \text{ nA m}^{-2}.$$

The current flow direction makes an angle of 58°.4 with the direction of the tube; thus, the projection of the current density to the tube-aligned direction $j_{\rm along} = 62.6$ nA m^{-2}, and the projection to the azimuthal direction is about $j_{\rm az} = 98.6$ nA m^{-2}. For this structure, the azimuthal current is about 50% higher than the tube-aligned current. The angle between the current flow direction and the upstream magnetic field is 60°.7. The field-aligned current with respect to the external magnetic field is also significantly smaller than the azimuthal one. The effective electric field, similarly to the previous structure, is ensured by the gradients of the ion pressure and the increase of the ion temperature. Efficient "collisions" similar to those described above may be ensured by the wave activity shown in Figure 11. The angle between the k-vector of the wave and the normal to the boundary estimated by MVA is 62°.5. The analysis of the characteristics of the trailing edge of this structure (see Figure 12) shows that the crossing duration was about 10 s, beginning from 17:06:26 until 16:06:36. The average velocity along the normal to the surface was about 55 km s^{-1}; thus, the characteristic width of the current sheet layer was about 550 km. The increment vector of the magnetic field

$$\delta\boldsymbol{B} = \boldsymbol{B}_{\rm after} - \boldsymbol{B}_{\rm inside} = [-92.3; -55.3; 8.45 - 13.2] \text{ nT}$$
$$|\delta\boldsymbol{B}| = 108.4 \text{ nT}.$$

An estimate of the current density gives the following result:

$$j = 157 \text{ nA m}^{-2}.$$

The normal component of the magnetic field is evaluated to be close to zero. The angle of the current axes with the axes of the tube is 64°.2, according to the following estimates for the parallel and azimuthal components of the current density:

$$j_{\rm par} = 69.1 \text{ nA m}^{-2}, \qquad j_{\rm az} = 141.3 \text{ nA m}^{-2}.$$

Here, the azimuthal component of the current is about twice as large as the normal component of the current. The current direction is approximately opposite to the current on the leading edge of the structure. An assumption that the current closure approximately takes place on the surface is validated similarly to the previous case. One can represent again the current element as quite an oblique ellipsoid crossing the structure under the corresponding angle of inclination that would generate the magnetic field perpendicular to it. The source of the electric field is again associated with the gradient of the ion pressure and ion density between the plasma inside and outside of the structure. The effective anomalous collisions that lead to the separation of electrons and ions motion are presumably determined by the surface wave activity, as in previous cases. Evaluating the global current direction ensuring the shear of the magnetic field, one can note that the inclination angle of the current element to the magnetic field axes makes an angle of 35°.5. Our data do not allow us to come to any detailed analysis of currents for the first event, because we have no information about the thickness of the current sheet. However, we can evaluate the angle of inclination of the global current with the axes of the magnetic tube, and we found it to be rather large, about 58°. The major characteristics of the two structures described above are summarized in Table 4.

Until now, our analysis was dedicated to the local properties of two typical relatively small magnetic structures, or switchbacks. The longer-duration structures often have a sufficiently more complicated form, including multiple substructures, which is why we have selected rather pure and simple cases to shed light on the local "design" of the tubes and to demonstrate the usefulness of the methods that may also be applicable for more complicated events. Our analysis certainly needs to be verified by a statistical study that will be presented in a separate publication. Our study provides reasonable support for the interpretation of the observed phenomena in terms of moving kinked magnetic tubes. Our approach is local; thus, it does not allow us to address many important issues, in particular: from where do the tubes originate? what causes the twisting of the tubes? is it forced by the collision with the solar-wind perturbations or it is produced due to the microinstability development? do the foot-point motions play any role in the formation of the magnetic-tube twists by means of meandering of the field lines, as was considered by Pommois et al. (2002), or may they be produced by some instability like a firehose or mirror? Further statistical studies on different distances closer to the Sun can provide more information to obtain answers to these questions. However, several features of the structures, namely, their similarity with the twisted field lines and enhanced parallel pressure inside, indicate that they are very similar to the twisted magnetic structures formed as a result of the Firehose instability. Hereafter, we consider some of its characteristics that may provide us with some key information leading to the interpretation of the observed physical phenomena.

4.3. Firehose Instability

Our analysis of the magnetic structures is based on in situ measurements during crossings of them by the satellite. On a larger scale, it is natural to suggest that the observed magnetic-field deviations from the surrounding field lines correspond to a deformation of the magnetic-field tube from a straight line to a twisted or kink type. The overwhelming majority of the flow is directed almost radially from the Sun, and the magnetic field lines are also close to the anti-radial direction, which supports a strong argument that these magnetic tubes are opened field lines. Enhanced parallel beta inside the structures with respect

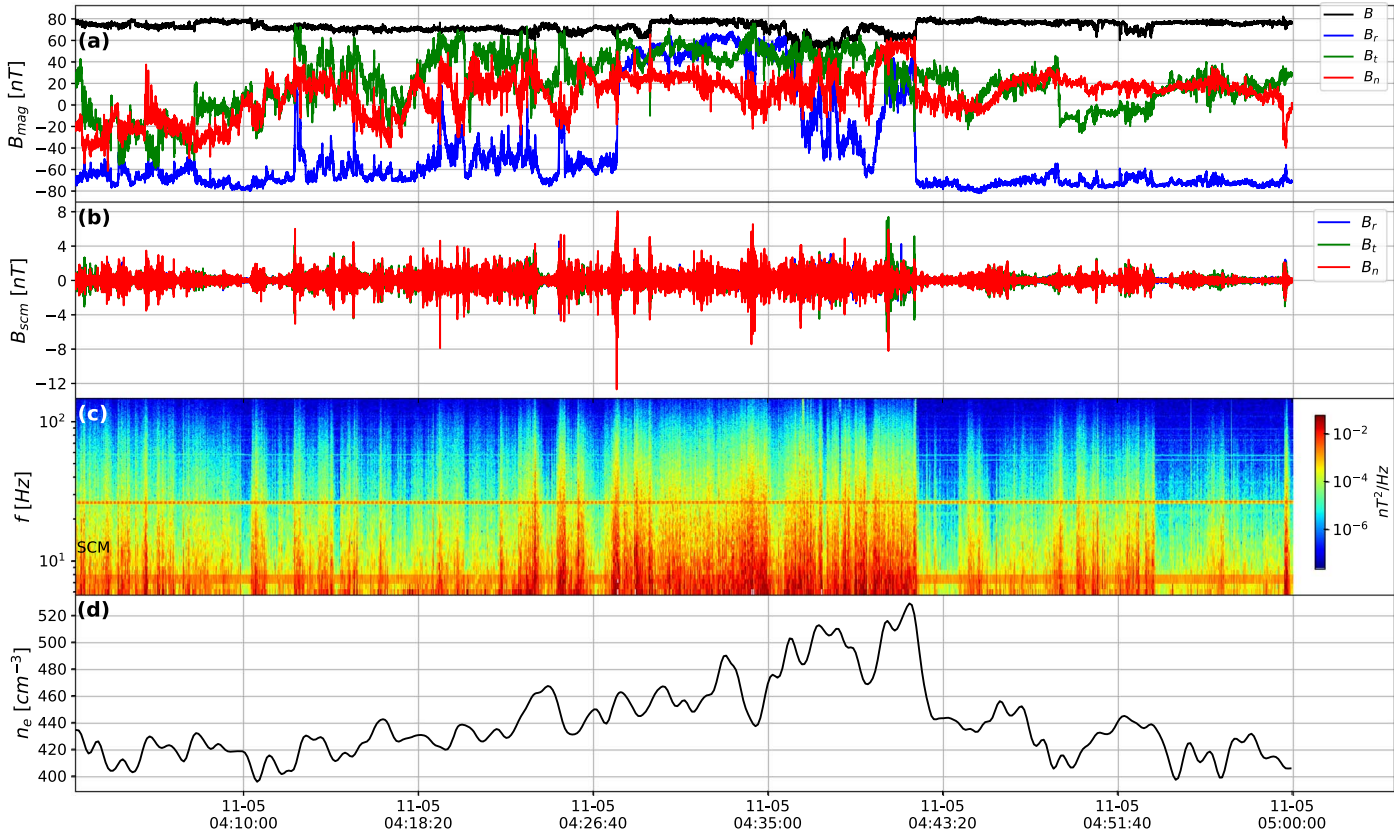

Figure 16. Structure containing the full reversal of the radial component of the magnetic field in the same format as in Figure 2.

to the surrounding plasma raises the question: may the evolution of the initially straight and almost radial magnetic tubes to a twisted and deformed configuration be caused by an instability of anisotropic ion distribution? The well-known instability that may result in such magnetic-tube deformation is the firehose instability discovered in late 1950s by Rosenbluth (1956), Vedenov & Sagdeev (1958), and Parker (1958). They determined the necessary and sufficient condition for the ion anisotropic instability to occur when the condition $\beta_{\|i} - \beta_{\perp i} > 2$ is satisfied. It was shown that due to it, there may grow two types of waves: the shear incompressible Alfvén waves and compressible Alfvén waves. These instabilities were studied in detail by many authors in different versions of Chew-Goldberg-Low (CGL) MHD and kinetic approximations (Shapiro & Shevchenko 1964; Kennel & Sagdeev 1967a, 1967b; Kennel & Scarf 1968; Berezin & Sagdeev 1969; Berezin 1972; Berezin & Vshivkov 1976; Gary 1993; Quest & Shapiro 1996; Gary et al. 1998; Horton et al. 2004). Statistical studies of the radial evolution of the solar wind from 0.3 to 1.0 au showed us that the ion distribution often consists of a core and a beam with relative velocity of the order of Alfvén speed (Marsch et al. 1982a; Marsch 2012). A simple analysis of the radial dependence of the plasma parameters based on double adiabatic invariants (CGL) approximation assuming that the magnetic field is radial and the density dependence upon the radius $\sim R^{-2}$, leads to a radial dependence of a perpendicular temperature $\sim R^{-2}$ and a parallel temperature constant (Matteini et al. 2011). This implies that the parallel beta increases with distance. However, experimental data are clearly in disagreement with the results of such analysis. Kasper et al. (2003) have shown that the temperature anisotropy is indeed constrained by thresholds of the microinstabilities. Matteini et al. (2011) concluded that there should exist parallel cooling and perpendicular heating. A strong support to the presence of these processes is provided by statistical analyses of the characteristic parallel and perpendicular temperatures and parameters of beta in a slow solar wind. It unambiguously shows that the distribution is limited in some area by curves corresponding to thresholds of firehose and mirror instabilities (Hellinger & TráVníčEk 2006; Bale et al. 2009). The kinetic study of these instabilities, including Hall and Finite Larmor Radius (FLR) corrections, resulted in a more accurate estimate of the threshold—it was found to be $\beta_{\|i} - \beta_{\perp i} \gtrsim 1.4$—and to the discovery of the instability of the oblique Alfvén wave mode (Hellinger & Matsumoto 2000, 2001; Wang & Hau 2003; Hau & Wang 2007). It was also found that the nonlinear saturation of the shear incompressible Alfvén-wave (it is also called the whistler type) instability occurs in a quasi-linear manner; namely, the wave amplitude reaches some finite value that corresponds to a decrease of the anisotropy. It is worth noting here that larger amplitudes would correspond to larger angular deviations and deformations of the field similar to those we observe inside the structures. This value is determined by the transition to the state of marginal stability; the instability is locked. After that, the amplitude of the wave slightly decreases and remains on this level slowly damping. This level corresponds to the condition of the marginal stability (Quest & Shapiro 1996; Gary et al. 1998; Hellinger & Matsumoto 2000, 2001; Matteini et al. 2006; Schekochihin et al. 2010). On the other hand, the evolution of the compressible wave is slightly different, the wave initially grows to some value and then decreases to some level of saturation, while the ratio of the perpendicular to parallel temperature grows to a significantly higher level than in the

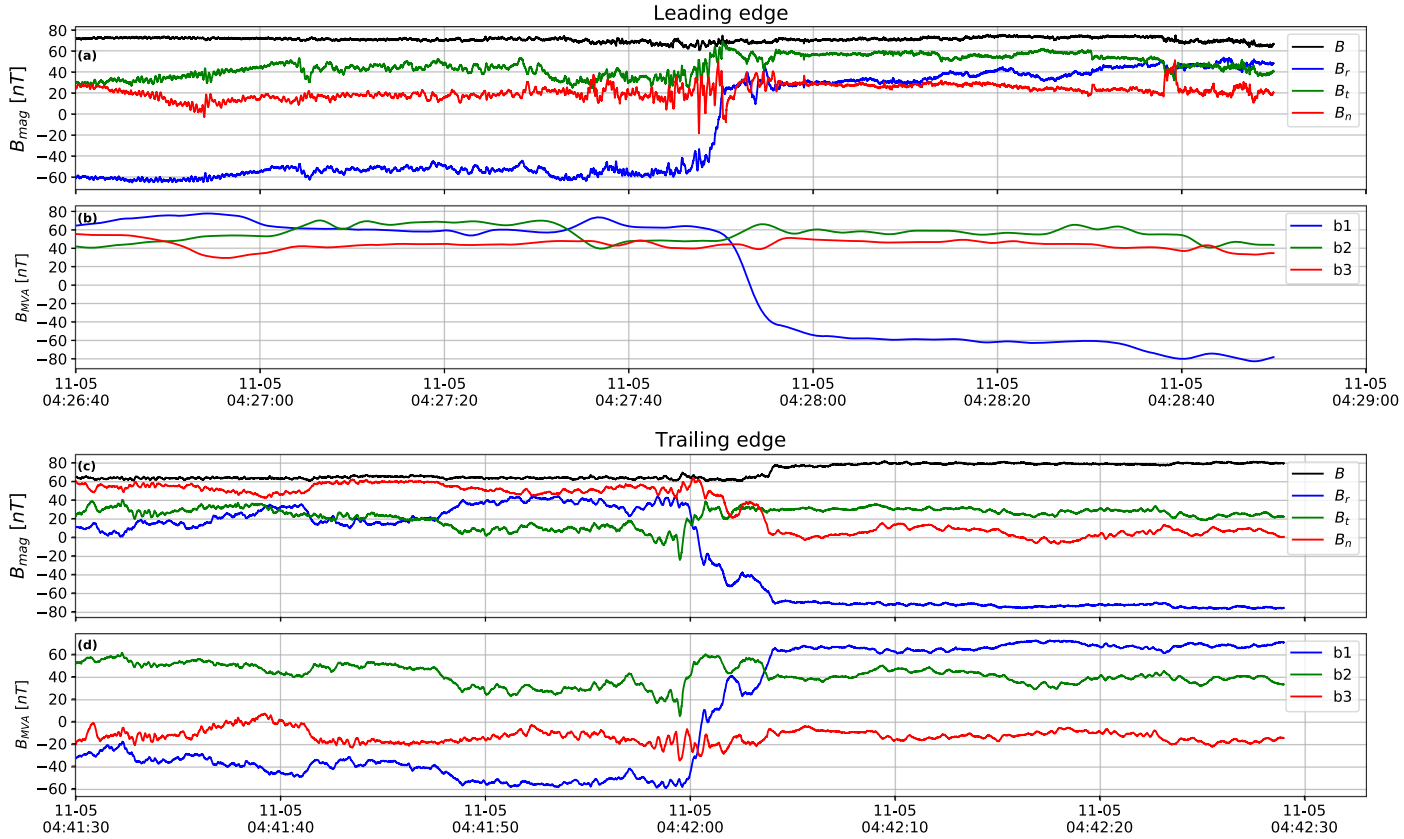

Figure 17. Magnetic field on the structure boundaries: the magnetic-field components on the leading edge in the RTN frame (a) and in the MVA frame (b); the magnetic field components on the trailing edge in the RTN frame (c) and in the MVA frame (d).

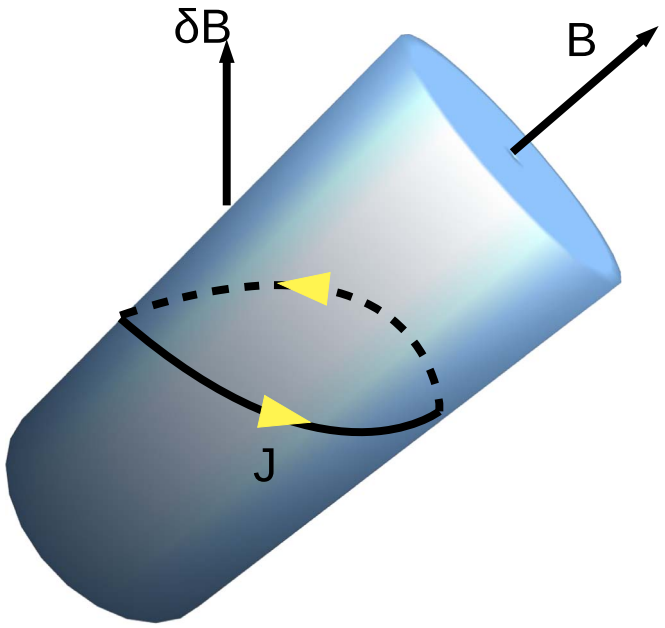

Figure 18. Geometry of the current system on the surface of the magnetic tube. Here, $\boldsymbol{B}$ is the magnetic-field vector directed along the axes of the magnetic tube; $\delta\,\boldsymbol{B} = \boldsymbol{B}_{\rm inside}$- $\boldsymbol{B}_{\rm outside}$ is the difference of magnetic field vectors inside and outside the tube. The elementary current loop on the surface in the plane perpendicular to $\delta\,\boldsymbol{B}$.

first case. It is reasonable to suggest that the two types of structures we analyzed here may represent the local manifestations of the tube deformations due to these two types of instability. Our observations supposedly correspond to a saturated stage of the instability development. Since the ion anisotropy may be produced due to two different mechanisms: (1) conservation of the adiabatic invariance and energy of particles while the magnetic field decreases with the distance from the Sun, and (2) the presence of the ion beam with the relative velocity larger than the Alfvén velocity. An important open question that requires a more detailed analysis of the ion distribution functions to be answered is: is the ion distribution monotonous or does it consist of a core and a beam or several beams, as was stated by Marsch et al. (1982a) and Marsch (2012), who analyzed the ion distributions registered on board Helios from 0.3 to 1 au? Assuming that on some distance closer to the Sun, ion anisotropy is provided by the presence of a distribution with a core and a beam, it is reasonable to suggest that the energy source for these structures may be provided by the jets in the low corona of the Sun that are often observed on the boundaries of the equatorial coronal holes (Nisticò et al. 2009; Raouafi et al. 2016). Such an assumption is supported by the long-range correlations between structures noted by Dudok de Wit et al. (2020). In the low corona, they have velocities of the order of 250–400 km s^{-1} (Nisticò et al. 2009; Paraschiv et al. 2010) and being combined with the bulk flow propagating outwards, may ensure the conditions for instability to be satisfied, since the Alfvén speed decreases with the radial distance. In such a picture, the macroscopic role of the observed magnetic structures, or switchbacks may consist of providing a mechanism of dissipation of energy supplied by the jets generated in the low corona.

Table 4
Characteristics of Boundary Layers of the Structures

Parameter	Alfvénic Structure	Compressional Structure
Characteristic perpendicular size of structure (km)	50,000	7000
Leading-edge (LE) thickness (km)	45	1000
LE current density (nA m^{-2})	1800	115
LE azimuthal current density (nA m^{-2})	950	115
LE tube-aligned current density (nA m^{-2})	1530	62
LE current density angle with tube axes (degrees)	29.8	58.4
Trailing-edge (TE) thickness km	440	550
TE current density (nA m^{-2})	165	157
TE azimuthal current density (nA m^{-2})	89	143
TE tube-aligned current density (nA m^{-2})	139	69.1
TE current density angle with tube axes (degrees)	32.7	62.4

5. Conclusion

Our analysis of three typical switchbacks with different characteristics suggests that these structures are magnetic flux tubes moving perpendicularly to their axis. They are filled with a "frozen in" plasma that flows along their local axial magnetic field. However, all of them have boundary layers in which the "frozen in" conditions are broken and strong currents flow. As a first-order approximation, these currents are closed on the boundary surface. An important property is their obliqueness with respect to the axis of the magnetic tube. The cross-section surface of the elementary current loop is perpendicular to the vector, representing a difference of magnetic fields inside and outside the structure. The surface boundary layer may vary from several tens of kilometers (which corresponds to several ion Larmor radii) to several hundred kilometers (considerably larger than the ion Larmor radius or the ion inertial length). In such circumstances, the surface may carry intense surface waves that have large angles with respect to the normal to the surface.

Another important feature of these switchbacks is the difference of ion beta inside and outside of the structure. This may in turn ensure the presence of the strong "effective" electric fields inside this layer associated with gradients of the plasma density and plasma temperature. Wave activity is confirmed by an analysis of the z-component of the Poynting flux (where z is close to the radial direction). All of these elements allow the system to remain quasi-stable and to evolve slowly, moving through the surrounding plasma. This last element may also modify the structure due to inhomogeneous forcing. The full reversals are probably produced by the deceleration of the deformed elements of the structure by the surrounding plasma.

The deflection of the magnetic field before and after crossing the switchback further reveals the existence of a total current that is carried by the structure. These deflections can be as large as 30°, which corresponds to changes in the vector magnetic field of about 20–30 nT. From these local characteristics, we conclude that these magnetic tubes are most likely twisted at larger scales. Such deformations of the magnetic-field lines qualitatively resemble marginally stable structures formed as a result of the development of the firehose instability.

The FIELDS experiment was developed and is operated under NASA contract NNN06AA01C. V.K., T.D., A.L., and C.F. acknowledge financial support of CNES in the frame of Parker Solar Probe grant. V.K. and O.A. were supported by NASA grant 80NSSC20K0697. V.K. and T.D. are grateful to P. Fergeau, M. Timofeeva, G. Jannet, P. Martin, M. Maksimovic, K. Amsif, and F. Gonzalez for their continuous support during the instrumental and scientific activities of the PSP project. S.D.B. acknowledges the support of the Leverhulme Trust Visiting Professorship programme. The Parker Solar Probe was designed, built, and is now operated by the Johns Hopkins Applied Physics Laboratory as part of NASA's Living with a Star (LWS) program (contract NNN06AA01C). Support from the LWS management and technical team has played a critical role in the success of the Parker Solar Probe mission. The data used in this study are available at the NASA Space Physics Data Facility (SPDF): https://spdf.gsfc.nasa.gov.

ORCID iDs

V. Krasnoselskikh https://orcid.org/0000-0002-6809-6219
A. Larosa https://orcid.org/0000-0002-7653-9147
O. Agapitov https://orcid.org/0000-0001-6427-1596
T. Dudok de Wit https://orcid.org/0000-0002-4401-0943
M. Moncuquet https://orcid.org/0000-0002-9621-0365
F. S. Mozer https://orcid.org/0000-0002-2011-8140
M. Stevens https://orcid.org/0000-0002-7728-0085
S. D. Bale https://orcid.org/0000-0002-1989-3596
J. Bonnell https://orcid.org/0000-0002-0675-7907
C. Froment https://orcid.org/0000-0001-5315-2890
K. Goetz https://orcid.org/0000-0003-0420-3633
P. Harvey https://orcid.org/0000-0002-6938-0166
J. Kasper https://orcid.org/0000-0002-7077-930X
R. MacDowall https://orcid.org/0000-0003-3112-4201
D. Malaspina https://orcid.org/0000-0003-1191-1558
M. Pulupa https://orcid.org/0000-0002-1573-7457
C. Revillet https://orcid.org/0000-0003-4582-7055
M. Velli https://orcid.org/0000-0002-2381-3106

References

Agapitov, O. V., Dudok de Wit, T., Mozer, F. S., et al. 2020, ApJL, 891, L20
Bale, S. D., Badman, S. T., Bonnell, J. W., et al. 2019, Natur, 576, 237
Bale, S. D., Goetz, K., Harvey, P. R., et al. 2016, SSRv, 204, 49
Bale, S. D., Kasper, J. C., Howes, G. G., et al. 2009, PhRvL, 103, 211101
Belcher, J. W., & Davis, L., Jr. 1971, JGR, 76, 3534
Berezin, I. A., & Vshivkov, V. A. 1976, JCoPh, 20, 81
Berezin, Y. A. 1972, JETP, 34, 998
Berezin, Y. A., & Sagdeev, R. Z. 1969, SPhD, 14, 62
Borovsky, J. E. 2016, JGRA, 121, 5055
Braginskii, S. I. 1965, RvPP, 1, 205
Burlaga, L. F., Lemaire, J. F., & Turner, J. M. 1977, JGR, 82, 3191
Coleman, P. J., Jr. 1968, ApJ, 153, 371

Denskat, K. U., Neubauer, F. M., & Schwenn, R. 1981, in Solar Wind 4 Conf. Proc., ed. H. Rosenbauer (Garching: Max-Planck-Institute für Aeronomie), 392
Dudok de Wit, T., Krasnoselskikh, V. V., Bale, S. D., et al. 2020, ApJS, 246, 39
Fox, N. J., Velli, M. C., Bale, S. D., et al. 2015, SSRv, 204, 7
Gary, S. P. 1993, Theory of Space Plasma Microinstabilities (Cambridge: Cambridge Univ. Press)
Gary, S. P., Li, H., O'Rourke, S., & Winske, D. 1998, JGR, 103, 14567
Gosling, J. T., McComas, D. J., Roberts, D. A., & Skoug, R. M. 2009, ApJL, 695, L213
Hau, L. N., & Wang, B. J. 2007, NPGeo, 14, 557
Hellinger, P., & Matsumoto, H. 2000, JGR, 105, 10519
Hellinger, P., & Matsumoto, H. 2001, JGR, 106, 13215
Hellinger, P., & TráVníčEk, P. 2006, JGRA, 111, A01107
Heyvaerts, J., & Priest, E. R. 1983, A&A, 117, 220
Hollweg, J. V. 1982, JGR, 87, 8065
Horbury, T. S., Matteini, L., & Stansby, D. 2018, MNRAS, 478, 1980
Horton, W., Xu, B. Y., Wong, H. V., & van Dam, J. W. 2004, JGRA, 109, A09216
Kasper, J. C., Abiad, R., Austin, G., et al. 2016, SSRv, 204, 131
Kasper, J. C., Bale, S. D., Belcher, J. W., et al. 2019, Natur, 576, 228
Kasper, J. C., Lazarus, A. J., Gary, S. P., & Szabo, A. 2003, in AIP Conf. Ser. 679, Solar Wind Ten, ed. M. Velli et al. (Melville, NY: AIP), 538
Kennel, C. F., & Sagdeev, R. Z. 1967a, JGR, 72, 3303
Kennel, C. F., & Sagdeev, R. Z. 1967b, JGR, 72, 3327
Kennel, C. F., & Scarf, F. L. 1968, JGR, 73, 6149
Landi, S., Hellinger, P., & Velli, M. 2005, in ESA Special Publication 592, Solar Wind 11/SOHO 16, Connecting Sun and Heliosphere, ed. B. Fleck, T. H. Zurbuchen, & H. Lacoste (Paris: ESA), 785
Landi, S., Hellinger, P., & Velli, M. 2006, GeoRL, 33, L14101
Marsch, E. 2006, LRSP, 3, 1
Marsch, E. 2012, SSRv, 172, 23
Marsch, E., Mohlhauser, K. H., Pilipp, W., Schwenn, R., & Rosenbauer, H. 1981a, in Solar Wind 4 Conf. Proc., ed. H. Rosenbauer (Garching: Max-Planck-Institute für Aeronomie), 443
Marsch, E., Rosenbauer, H., Schwenn, R., Muehlhaeuser, K. H., & Denskat, K. U. 1981b, JGR, 86, 9199
Marsch, E., Rosenbauer, H., Schwenn, R., Muehlhaeuser, K. H., & Neubauer, F. M. 1982a, JGR, 87, 35
Marsch, E., Schwenn, R., Rosenbauer, H., et al. 1982b, JGR, 87, 52
Matteini, L., Hellinger, P., Goldstein, B. E., Land i, S., & Velli, M. M. 2011, AGUFM, 2011, SH53B-2041
Matteini, L., Horbury, T. S., Neugebauer, M., & Goldstein, B. E. 2014, GeoRL, 41, 259
Matteini, L., Landi, S., Hellinger, P., & Velli, M. 2006, JGRA, 111, A10101
Meyer-Vernet, N., Issautier, K., & Moncuquet, M. 2017, JGRA, 122, 7925
Moncuquet, M., Meyer-Vernet, N., Issautier, K., et al. 2020, ApJS, 246, 44
Mozer, F. S., Agapitov, O. V., Bale, S. D., et al. 2020, ApJS, 246, 68
Neubauer, F. M., & Barnstorf, H. 1981, in Solar Wind, ed. H. Rosenbauer (Garching: Max-Planck-Institute für Aeronomie), 168
Neugebauer, M. 2013, SSRv, 176, 125
Nisticò, G., Bothmer, V., Patsourakos, S., & Zimbardo, G. 2009, SoPh, 259, 87
Paraschiv, A. R., Lacatus, D. A., Badescu, T., et al. 2010, SoPh, 264, 365
Parker, E. N. 1958, PhRv, 109, 1874
Pommois, P., Veltri, P., & Zimbardo, G. 2002, in ESA Special Publication 477, Solspa 2001, Proceedings of the Second Solar Cycle and Space Weather Euroconference, ed. H. Sawaya-Lacoste (Paris: ESA), 305
Quest, K. B., & Shapiro, V. D. 1996, JGR, 101, 24457
Raouafi, N. E., Patsourakos, S., Pariat, E., et al. 2016, SSRv, 201, 1
Rosenbluth, M. 1956, Tech. Rep., Los Alamos Sci. Lab. Rep. LA2030
Sonnerup, B. U. Ö., & Scheible, M. 1998, ISSIR, 1, 185
Schekochihin, A. A., Cowley, S. C., Rincon, F., & Rosin, M. S. 2010, MNRAS, 405, 291
Shapiro, V. D., & Shevchenko, V. 1964, Sov. Phys. JETP, 18, 1109
Suess, S. T. 2007, in ESA Special Publication 641, Second Solar Orbiter Workshop, ed. E. Marsch et al. (Noordwijk: ESA), 11
Vedenov, A., & Sagdeev, R. 1958, SPhD, 3, 278
Wang, B. J., & Hau, L. N. 2003, JGRA, 108, 1463
Yamauchi, Y., Suess, S. T., Steinberg, J. T., & Sakurai, T. 2004, JGRA, 109, A03104